HHS Public Access

Author manuscript

Cell. Author manuscript; available in PMC 2021 June 25.

Published in final edited form as:

Cell. 2020 June 25; 181(7): 1612–1625.e13. doi:10.1016/j.cell.2020.05.017.

Intratumoral CD4+ T cells mediate anti-tumor cytotoxicity in human bladder cancer

David Y. Oh[1,10], **Serena S. Kwek**[1,10], **Siddharth S. Raju**[3,6,8], **Tony Li**[1], **Elizabeth McCarthy**[3], **Eric Chow**[4], **Dvir Aran**[5], **Arielle Ilano**[1], **Chien-Chun Steven Pai**[1,11], **Chiara Rancan**[1], **Kathryn Allaire**[1], **Arun Burra**[1], **Yang Sun**[3], **Matthew H. Spitzer**[2,6,8], **Serghei Mangul**[9], **Sima Porten**[7], **Maxwell V. Meng**[7], **Terence W. Friedlander**[1], **Chun Jimmie Ye**[2,3,*], **Lawrence Fong**[1,2,12,*]

[1.]Division of Hematology/Oncology, Cancer Immunotherapy Program, University of California, San Francisco, CA 94143, USA;

[2.]Parker Institute for Cancer Immunotherapy, University of California, San Francisco, CA 94143, USA;

[3.]Department of Epidemiology and Biostatistics and Institute for Human Genetics, University of California, San Francisco, CA 94143, USA;

[4.]Department of Biochemistry and Biophysics, Center for Advanced Technologies, University of California, San Francisco, CA 94143, USA;

[5.]Bakar Computational Health Sciences Institute, University of California, San Francisco, CA 94143, USA;

[6.]Department of Microbiology and Immunology, University of California, San Francisco, CA 94143, USA;

[7.]Department of Urology, University of California, San Francisco, CA 94143, USA;

[8.]Department of Otolaryngology - Head and Neck Surgery, University of California, San Francisco, CA 94143, USA;

[9.]Department of Computer Science, University of California, Los Angeles, CA 90095, USA.

[10.]These authors contributed equally.

[*]Correspondence: Lawrence Fong (lawrence.fong@ucsf.edu) and Chun Jimmie Ye (jimmie.ye@ucsf.edu).

Author Contributions

Study concept and design: D.Y.O., S.S.K., L.F.

Acquisition of patients, samples, data: D.Y.O., S.S.K., A.I., C.-C.P., C.R., K.A., A.B., S.P., M.V.M., T.W.F.

Data analysis and interpretation: D.Y.O., S.S.K., S.S.R., T.L., E.M., E.C., D.A., A.I., K.A., A.B., Y.S., M.H.S., S.M., C.J.Y., L.F.

Writing of manuscript: D.Y.O., S.S.K., C.J.Y, L.F.

Study oversight: C.J.Y., L.F.

Declaration of Interests

D.Y.O. has received research support from Roche/Genentech and Merck, and has served as a paid consultant for Maze Therapeutics.

L.F. has received research support from Roche/Genentech, Abbvie, Bavarian Nordic, Bristol Myers Squibb, Janssen, and Merck.

C.J.Y. is a co-founder of Dropprint Genomics.

[11]Current address: Department of Oncology Biomarker Development, Genentech, 1 DNA Way, South San Francisco, CA 94080

[12]Lead Contact

Summary

Responses to anti-PD-1 immunotherapy occur but are infrequent in bladder cancer. The specific T cells that mediate tumor rejection are unknown. T cells from human bladder tumors and non-malignant tissue were assessed with single-cell RNA and paired T cell receptor (TCR) sequencing of 30,604 T cells from 7 patients. We find that the states and repertoire of $CD8^+$ T cells are not altered in tumors compared to non-malignant tissues. In contrast, single-cell analysis of $CD4^+$ T cells demonstrate several tumor-specific states including multiple distinct states of regulatory T cells. Surprisingly, we also find multiple cytotoxic $CD4^+$ T cell states, which are clonally expanded. These CD4+ T cells can kill autologous tumor in an MHC class II dependent fashion and are suppressed by the regulatory T cells. Further, a gene signature of cytotoxic $CD4^+$ T cells in tumors predicts clinical response in 244 metastatic bladder cancer patients treated with anti-PD-L1.

Graphical Abstract

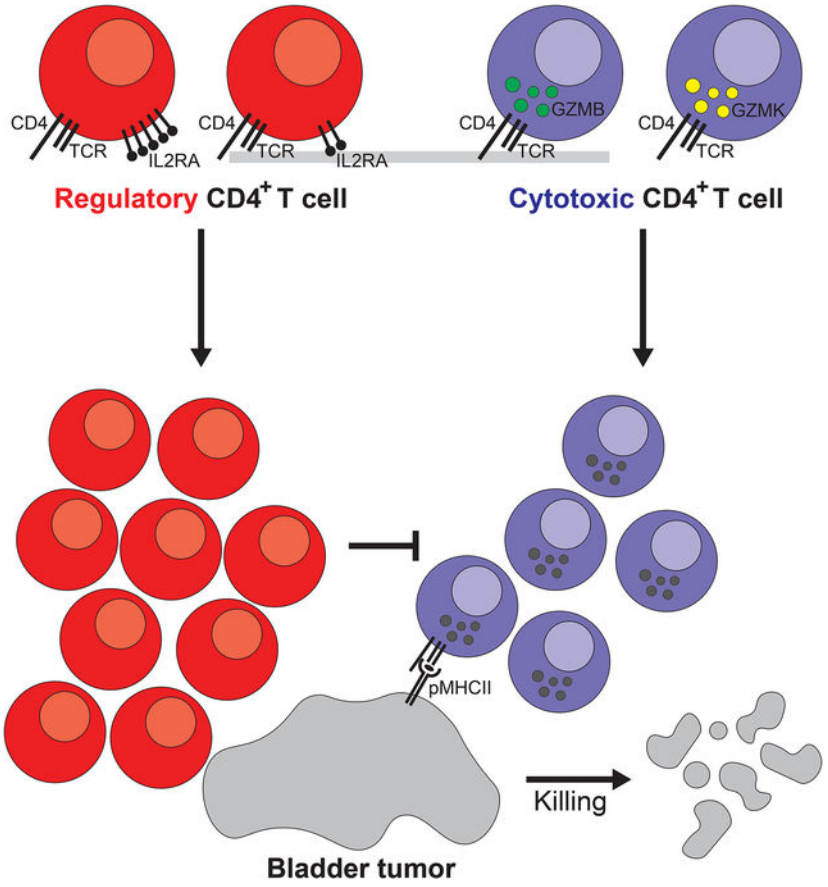

In brief

Single-cell RNA and paired T cell receptor sequencing highlights the enrichment of cytotoxic CD4+ T cells, rather than CD8+ T cells, in human bladder cancer. These CD4+ T cells are capable of killing autologous tumor cells and are subjected to inhibition by Tregs.

Keywords

Bladder cancer; checkpoint inhibition; PD-1 blockade; anti-PD-L1; single-cell sequencing; cytotoxic $CD4^+$ T cells; predictive gene signature

Introduction

Immunotherapies have changed the landscape of cancer treatment by producing durable and long-lasting responses through triggering of anti-tumor cell-mediated immunity. In particular, checkpoint inhibitors (CPI) targeting immune inhibitory molecules CTLA-4 and PD-1 in T lymphocytes have been approved based on responses and improved overall survival in multiple malignancies, particularly those with high mutational burden (Hodi et al., 2010; Herbst et al., 2014; Powles et al., 2014; Robert et al., 2015; Martincorena and Campbell, 2015; Cancer Genome Atlas Research Network, 2008). However, in specific malignancies such as transitional cell carcinoma (TCC) of the bladder, CPIs as monotherapies are efficacious in only ~20% of patients (Powles et al., 2014; Hargadon et al., 2018). This could be partly due to the heterogeneity of tumor-infiltrating T lymphocytes (TILs) and their differential ability to confer a therapeutic benefit upon treatment.

Currently, cytotoxic $CD8^+$ T cells are the main focus of efforts to understand how immunotherapy elicits anti-tumor immunity. In melanoma, expression and chromatin state signatures of cytotoxicity and exhaustion (Tirosh et al., 2016; Philip et al., 2017; Ayers et al., 2017; Herbst et al., 2014) and the presence of $CD8^+$ T cells at the tumor invasive margin pre-treatment (Tumeh et al., 2014) are significantly correlated with subsequent responses to PD-1-directed therapy. However, in metastatic bladder TCC, where response rates to PD-1 blockade are ~15–20% in platinum chemotherapy-refractory patients and >20% in frontline platinum-ineligible patients, predictive biomarkers of response are unclear, including PD-L1 expression (Koshkin and Grivas, 2018). Recently, bulk RNA sequencing (RNA-seq) of the pre-treatment tumor microenvironment in TCC found that a higher score of $CD8^+$ gene signature and tumor mutational burden, and conversely a lower score of transforming growth factor-beta (TGF-β) gene signature particularly in immune excluded tumors, were associated with response to the anti-PD-L1 agent atezolizumab (Mariathasan et al., 2018). However, the importance of heterogeneous subsets of TILs in TCC beyond canonical $CD8^+$ cytotoxic and exhausted phenotypes in responses to PD-1 blockade remains unexplored. In particular, the role of $CD4^+$ T cells in either controlling or enhancing TCC tumor growth remains largely unknown. While regulatory $CD4^+$ T cells (Tregs) in the TCC environment have been associated with adverse outcomes (Baras et al., 2016), and a $CD4^+$ subset expressing inducible costimulator (ICOS) that produces interferon-gamma (IFNγ) in response to anti-CTLA-4 therapy has been described in human bladder tumors (Liakou et al. 2008), the presence of other $CD4^+$ T cells subsets that directly promote cell-mediated immunity through other effector mechanisms remains unclear. Detailed characterization of the T

lymphocytes in the tumor is critically needed for precisely mapping the cells responsible for tumor recognition and control and defining predictive markers of response to CPI in bladder cancer.

To address these points, we interrogated the tumor microenvironment of patients with localized muscle-invasive bladder TCC, who either received or did not receive neoadjuvant anti-PD-L1 immunotherapy (atezolizumab, Roche/Genentech) prior to surgical resection. Droplet single-cell RNA-sequencing (dscRNA-seq) and paired TCR sequencing of > 30,000 $CD4^+$ and $CD8^+$ T cells from paired tumor and adjacent non-malignant tissues revealed heterogeneity in known $CD4^+$ states such as regulatory T cells, which were also enriched and clonally expanded in tumor. In addition, several states of cytotoxic $CD4^+$ T cells expressing cytolytic effector proteins were identified, some of which are enriched in tumor. Cytotoxic $CD4^+$ T cells were clonally expanded in tumor and could kill autologous tumor *ex vivo*. Cytotoxic $CD4^+$ T cells existed in discrete proliferating and non-proliferating states in tumor. A gene signature of cytotoxic $CD4^+$ T cells was predictive of response to PD-1 blockade in an orthogonal RNAseq dataset of metastatic bladder cancer patients treated with anti-PD-L1. Overall these findings highlight the importance of $CD4^+$ T cell heterogeneity and the relative balance between activation of cytotoxic $CD4^+$ effectors and inhibitory regulatory cells for killing of autologous tumor.

Results

Canonical $CD8^+$ T cell states were not enriched in the bladder tumor microenvironment.

To assess the T cell composition of the tumor environment, we profiled T cells from dissociated bladder tumors and adjacent uninvolved bladder tissues using single-cell RNA and TCR sequencing (schematic in Figure S1A). We used the 10X Genomics Chromium platform (Zheng et al., 2017) to sequence 8,833 tumor- and 1,929 non-malignant-derived $CD8^+$ T cells from 7 patients (Table S1). All samples were muscle-invasive bladder cancer (MIBC) from: 2 standard-of-care untreated patients (“untreated”), 1 chemotherapy-treated patient (gemcitabine + carboplatin, “chemo”), and 4 anti-PD-L1-treated patients (“anti-PD-L1”) with detailed clinical annotations (Table S1). To assess the shared heterogeneity of T cells across samples, we restricted the analysis to highly variable genes and used an empirical bayes approach (ComBat, Johnson et al., 2007; Büttner et al., 2019) to account for preparation batch among individual samples. We subsequently used leiden clustering (Traag et al., 2019) to define clusters which were visualized using Uniform Manifold Approximation and Projection (UMAP) (McInnes and Healy, 2018). Tumor- and non-malignant-derived $CD8^+$ T cells form 11 clusters each populated by cells from all samples suggestive of shared states in TCC regardless of the treatment regimen (Figure 1A, Figure S2A). Differential expression analyses comparing each cluster to all other cells combined identified 1067 differentially expressed genes in at least one cluster ($P_{adj} < 0.05$, $|\log_2(FC)| > 0.5$) (Table S2). The identified states include known $CD8^+$ subtypes (Figure 1B–C): cells expressing *HAVCR2* (TIM-3), *LAG3*, *ENTPD1*, as well as the chemokine *CXCL13* ($CD8_{ENTPD1}$: $\log_2(FC) = 1.4–3.7$) previously described as tumor-reactive $CD8^+$ T cells (Duhen et al., 2018); effector cells expressing *FGFBP2* and *GNLY*, which is a granule-associated pore-forming protein known to function in pathogen killing (Krensky and

Clayberger, 2009) ($CD8_{FGFBP2}$: $log_2(FC) = 3.6–5.3$); naïve cells expressing *CCR7* and *GZMK* ($CD8_{NAIVE}$: $log_2(FC) = 0.9–2.8$); central memory cells expressing both *CCR7* and *SELL* (L-selectin) ($CD8_{CM}$: $log_2(FC) = 1.5–1.7$); and mucosal-associated invariant cells expressing *KLRB1* ($CD8_{MAIT}$: $log_2(FC) = 2.7$) that preferentially use the known semi-invariant TCR alpha chains TRAV1–2/TRAJ33 (Kurioka et al., 2016) (Figure 1D). Of note, we also found *MKI67*$^+$ proliferating cells ($CD8_{PROLIF}$: $log_2(FC) = 6.5$) as well as cells expressing the chemokines *XCL1/2* ($CD8_{xcl}$: $log_2(FC) = 5.2–5.6$). Similar states were also identified in the tumor environment of hepatocellular carcinoma based on scRNA-seq (Zheng et al., 2017a). Surprisingly, although the frequency of $CD8_{ENTPD1}$ cells were higher in tumors, none of the $CD8^+$ states displayed statistically significant differences in frequency between the tumor and non-malignant bladder (exact permutation test, Figure 1E; density plots in Figure 1F).

Regulatory $CD4^+$ T cells (Tregs) included heterogeneous states which are enriched in bladder tumors.

Given the lack of tumor enrichment of $CD8^+$ states and the higher frequency of $CD4^+$ over $CD8^+$ T cells in bladder tumors (Figure S1B), we investigated $CD4^+$ T cell heterogeneity in a similar fashion to determine their contribution to anti-tumor responses. We sequenced and analyzed 16,995 tumor- and 2,847 non-malignant-infiltrating $CD4^+$ T cells isolated from the same patients. Tumor- and non-malignant-derived $CD4^+$ T cells form 11 clusters each with representation from all individual patients (Figure 2A; Figure S2B). We identified 1511 differentially expressed genes in at least one cluster ($P_{adj} < 0.05$, $|log_2(FC)| > 0.5$, Table S2, Figure 2B–C) defining several canonical $CD4^+$ T cell states. These include *CCR7*$^+$ cells, which demonstrated a central memory phenotype ($CD4_{CM}$) based on parallel flow cytometry data showing these are $CD45RA^-$ (see below), as well as cells expressing high levels of *CXCL13* and *IFNG* ($CD4_{CXCL13}$: $log_2(FC) = 5.9$ and 1.4), which are also likely to be exhausted based on overexpression of *TOX* ($log_2(FC) = 1.9$) (Yao et al., 2019) and whose presence has been associated with improved outcomes in breast, gastric, and microsatellite-unstable colorectal carcinoma which is an immune-responsive tumor (Schmidt et al., 2018; Gu-Trantien et al., 2013; Gu-Trantien et al., 2017; Wei et al., 2018; Zhang et al., 2018). Other states included Th17 cells expressing *IL17A* ($CD4_{TH17}$: $log_2(FC) = 4.7$), which represented important anti-tumor effectors (Kryczek et al., 2011), activated cells expressing *CD69* ($CD4_{ACTIVATED}$: $log_2(FC) = 2.2$) but not *FOXP3* ($log_2(FC) < 0.5$) (Figure 2B–C); as well as several important additional states described in further detail below. Notably some of these states were selectively enriched in specific compartments. $CD4_{CXCL13}$ demonstrated significant enrichment in tumor compared to non-malignant tissue (tumor vs non-malignant: 6.5 vs 3.0%, P = 0.015, exact permutation test), while states enriched in non-malignant tissue included $CD4_{CM}$ (tumor vs non-malignant: 30 vs 42%, P = 0.008) and $CD4_{ACTIVATED}$ (tumor vs non-malignant: 7.5 vs 10%, P = 0.02) (density plots in Figure 2D; tumor and non-malignant frequencies in Figure 2E).

Tregs were an abundant constituent of the bladder tumor microenvironment with demonstrated heterogeneity. We found two states of Tregs ($CD4_{IL2RAHI}$ and $CD4_{IL2RALO}$) together constituting 26 ± 1.9% (mean ± s.e.m.) of tumor-infiltrating $CD4^+$ cells, which co-expressed *FOXP3* ($CD4_{IL2RAHI}$: $log_2(FC) = 2.7$; $CD4_{IL2RALO}$: $log_2(FC) = 1.2$) and known

immune checkpoints including *IL2RA, TIGIT, TNFRSF4/9/18* and *CD27* (Philip et al., 2017; Zheng et al., 2017a; Plitas et al., 2016; De Simone et al., 2016) ($CD4_{IL2RAHI}$ and $CD4_{IL2RALO}$: $log_2(FC) > 0.65$; Figure 2B–C, Figure 3A). With the exception of *TIGIT*, these immune checkpoints are minimally expressed by other $CD4^+$ states such as $CD4_{CM}$ (Figure 3A). The two Treg states were distinguished by higher expression of *IL2RA*, *TNFRSF4*, *TNFRSF9*, and *TNFRSF18* in $CD4_{IL2RAHI}$ cells ($CD4_{IL2RAHI}$: $log_2(FC) = 2.5–3.6$; $CD4_{IL2RALO}$: $log_2(FC) = 0.4–1.6$; Figure 3A, Table S2). Of note, both Treg states were significantly enriched in tumor compared to adjacent non-malignant tissue ($CD4_{IL2RAHI}$: 14.3 vs 4.6%, P = 0.002; $CD4_{IL2RALO}$: 11.1 vs 6.7%, P = 0.002; exact permutation test, Figure 2E). We confirmed by flow cytometry from 7 additional bladder tumors that multiple tumors contain distinct regulatory states that express graded protein levels of IL2RA, and co-express significantly different levels of immune checkpoints such as TNFRSF18 ($P < 0.05$ for TNFRSF18 expression in $FOXP3^+$ $CD25^{low}$ versus $CD25^{hi}$ populations by Wilcoxon signed-ranked test, Figure 3B, gating strategy in Figure S1C–D). This heterogeneity may be consequential as Tregs expressing higher levels of immune checkpoints have been shown to be correlated with poorer outcomes in non-small cell lung cancer (Guo et al., 2018). Both regulatory states also demonstrated a common tumor-specific gene expression program, which included several heat shock proteins compared to non-malignant tissue (Figure S2C, Table S2).

Tregs are clonally expanded in bladder tumors.

To query the TCR sequence in the same single cells for which we obtained whole-transcriptome data, we PCR-amplified and sequenced to saturation the complementarity-determining region 3 (CDR3) of the TCR alpha (TRA) and beta (TRB) loci from the barcoded full-length cDNA library (primers in Table S3). After filtering for matching whitelisted cell barcodes (Cell Ranger), this approach yielded 11,081 $CD4^+$ T cells and 5,779 $CD8^+$ T cells with paired TRA and TRB CDR3 sequences (49% and 47% recovery, respectively; summary in Table S3). These results are consistent with expected frequencies based on the average recovery of individual TRA ($CD4^+$: 54%, $CD8^+$: 50%) and TRB ($CD4^+$: 68%, $CD8^+$: 67%) sequences across whitelisted cells. Overall, the TCR repertoire was more restricted in the tumor microenvironment than adjacent non-malignant tissue based on two analyses. First, in intratumoral $CD4^+$ T cells, 10.8 ± 1.6% of unique clonotypes are shared by 2 or more cells; this degree of sharing was significantly greater than in the non-malignant compartment (5.1 ± 1.6%; unpaired T-test, P = 0.033), and is not seen in blood from healthy donors (0.12–0.16%) or from publicly available reference circulating $CD4^+$ T cell data (0%) (Figure S3A). Second, we observed a skewing of the intratumoral $CD4^+$ T cell repertoire towards an increased cumulative frequency of clonotypes over fewer cells (Figure S3B) and a corresponding higher Gini coefficient (0.21 for tumor vs 0.05 for non-malignant, Wilcoxon signed-rank test with Benjamini-Hochberg correction, P = 0.009, Figure S3C) compared to the non-malignant compartment and healthy controls.

When we assigned TCR sequences to cells with cluster identities (9,770 $CD4^+$ and 5,151 $CD8^+$ T cells with a paired TRA/TRB had an assigned phenotypic cluster in scanpy, or 49% and 48% of all T cells with assigned clusters, respectively; merged TCR sequences and

phenotypic clusters for $CD4^+$ and $CD8^+$ T cells in Tables S4), we found that clonal expansion of Tregs contributes to intratumoral $CD4^+$ T cell repertoire restriction. Compared to paired non-malignant tissue, both regulatory states exhibited increased Gini coefficients in tumor ($CD4_{IL2RAHI}$: $Gini_{tumor}$ 0.17 vs $Gini_{normal}$ 0, P = 0.003, $CD4_{IL2RALO}$: $Gini_{tumor}$ 0.06 vs $Gini_{normal}$ 0.003, P = 0.009, exact permutation test, Figure 3C). The most expanded clonotypes within the Tregs were specific to regulatory cells and not other cell states (all single cells expressing the top expanded regulatory clonotypes shown in Figure 3D). The *CXCL13*-expressing state $CD4_{cxcl13}$ (discussed in greater detail below) also was restricted in tumor ($Gini_{tumor}$ 0.07 vs $Gini_{normal}$ 0, P = 0.02, exact permutation test, Figure 3C). Gini coefficients for $CD4^+$ states did not differ significantly by anti-PD-L1 treatment (Figure S3G). By contrast, although repertoire restriction was also seen in $CD8^+$ T cells from the same samples, this is observed in both tumor (% unique clonotypes shared between cells: 15.1 ± 1.1%; $Gini_{tumor}$: 0.36 ± 0.04) and non-malignant compartments (% unique clonotypes shared between cells: 14.6 ± 0.2%; $Gini_{normal}$: 0.39 ± 0.06; Figure S3D–F). Furthermore, no significant increase in Gini coefficient in tumor over non-malignant tissue was seen for any $CD8^+$ state, including with anti-PD-L1 treatment (Figure S3H–I). Hence an important contributor to increased repertoire restriction of tumor-infiltrating $CD4^+$ over non-malignant tissue, which was not seen in the $CD8^+$ compartment, involved clonal expansion of several distinct regulatory T cell states that differed in their levels of immune checkpoint expression, which may be driven by tumor-associated antigens and the tumor-specific microenvironment.

Bladder tumors possessed multiple cytotoxic $CD4^+$ T cell states.

In addition to regulatory states, we also found 2 distinct states of cytotoxic $CD4^+$ T cells in all samples constituting 15 ± 0.9% of tumor-infiltrating $CD4^+$ T cells. Both the $CD4_{GZMB}$ and $CD4_{GZMK}$ cytotoxic cells expressed a core set of cytolytic effector molecules ($log_2(FC) > 0.5$, $P_{adj} < 0.05$): *GZMA* (granzyme A), *GZMB* (granzyme B), and *NKG7* (a granule protein that translocates to the surface of NK cells following target cell recognition [Medley et al., 1996]) (Figure 2B–C, Figure 4A, Table S2). Each cytotoxic $CD4^+$ state was distinguished by the expression of specific effector molecules: $CD4_{GZMB}$ cells co-expressed high levels of *GZMB*, the pore-forming protein *PRF1* (perforin), and the granule-associated proteins *GNLY* and *NKG7* ($CD4_{GZMB}$: $log_2(FC)$ = 5.7, 3.4, 5.1, 4.4 respectively), while $CD4_{GZMK}$ cells co-expressed high levels of the distinct granzyme *GZMK* and lower levels of *NKG7* ($CD4_{GZMK}$: $log_2(FC)$ = 6.3 and 3.9) (Figure 4A, Table S2). These shared cytolytic molecules were not expressed by other $CD4^+$ states including regulatory and central memory T cells (Figure 4A). Cytotoxic $CD4^+$ cells co-expressed additional molecules, which may further contribute to anti-tumor effector function: notably *IFNG* was expressed by both cytotoxic states, which may contribute to tumor cell death including ferroptosis (Wang et al., 2019) ($CD4_{GZMB}$ and $CD4_{GZMK}$: $log_2(FC)$ = 2.1). Of note, the minority of $CD4_{GZMB}$ cells that expressed *IFNG* appeared to also express *TNF* as well as specific immune checkpoints such as *PDCD1*, *LAG3*, and *HAVCR2* (TIM3) (Figure 4A). A larger proportion of $CD4_{GZMB}$ cells expressed *CXCR6* ($CD4_{GZMB}$: $log_2(FC)$ = 1.3, Figure 4A). This chemokine is expressed in both regulatory and non-regulatory $CD4^+$ TILs from colorectal carcinoma, nasopharyngeal carcinoma, and renal cell carcinoma, and together with its ligand *CXCL16*, can mediate TIL chemotaxis (Löfroos et al., 2017; Parsonage et al., 2012; Oldham et al.,

2012). Finally, the $CD4_{GZMB}$ and $CD4_{GZMK}$ cells did not express high levels of other checkpoints associated with regulatory T cells such as *IL2RA*, *TIGIT*, or *TNFRSF4/9/18* ($log_2(FC) < 0.5$, Figure 4A), nor did they express the exhaustion marker *TOX* (Table S2). Similar states were found with unbiased clustering without batch correction for paired tumor- and non-malignant-derived $CD4^+$ cells from individual patients (Figure S2D–E).

We validated the presence and functional heterogeneity of cytotoxic $CD4^+$ T cells using several orthogonal and complementary methods. Using flow cytometry, the presence of cytotoxic $CD4^+$ T cells with an effector memory ($CCR7^-$ $CD45RA^-$) or effector ($CCR7^-$ $CD45RA^+$) phenotype that express GZMB, GZMK, and perforin protein was confirmed by flow cytometry in tumors from multiple independent replicate samples (N = 7 tumors, Figure 4B, gating strategy in Figure S1C–D). Across this sample set, 9 ± 2.9% (mean ± s.e.m.) of $CD4^+$ $FOXP3^-$ $CCR7^-$ cells expressed GZMB, while 16 ± 4.5% expressed GZMK and 5.3 ± 2.6% expressed perforin (Figure 4C, left panel), at lower frequencies than $CCR7^-$ $CD8^+$ cytotoxic cells from the same patients (Figure S1E–G). Importantly, 25.9 ± 8.7% of $GZMB^+$ $CD4^+$ $FOXP3^-$ $CCR7^-$ and 8.6 ± 3.5% of $GZMK^+$ $CD4^+$ $FOXP3^-$ $CCR7^-$ cytotoxic T cells showed co-expression of perforin with granzymes, in agreement with the scRNA-seq data (Figure 4C, right panel); these frequencies of granzyme and perforin co-expression were lower than $CCR7^-$ $CD8^+$ cytotoxic cells from the same patients (Figure S1F–G). Importantly, $CD45^-$ bladder tumor cells express multiple MHCII molecules (data not shown), which would allow for antigen recognition by TCRs expressing CD4 as a co-receptor. Flow cytometry of a separate set of 11 muscle-invasive bladder tumors confirms the functional capacity of cytotoxic $CD4^+$ T cells to produce multiple cytokines; in agreement with the scRNA-seq data, 56 ± 4.8% (mean ± s.e.m.) of $CD4^+$ $CCR7^-$ cells were polyfunctional and could produce both IFNγ and TNFα, while a minority of these cells only secrete IFNγ alone or TNFα alone after stimulation and therefore may demonstrate signs of exhaustion ($IFN\gamma^+$ $TNFa^-$: 2.0 ± 0.76%; $IFN\gamma^-$ $TNF\alpha^+$: 19 ± 3.3%) (Figure 4D–E). The frequency of polyfunctional cytotoxic $CD4^+$ T cells was similar to stimulated $CD8^+$ $CCR7^-$ T cells from the same patients ($IFN\gamma^+$ $TNF\alpha^+$: 55 ± 6.3%), although $CD8^+$ $CCR7^-$ T cells that were monofunctional demonstrated an increased trend towards preferential IFNγ production alone over TNFα production compared to cytotoxic $CD4^+$ T cells ($IFN\gamma^+$ $TNF\alpha^-$: 14 ± 4.7%; $IFN\gamma^-$ $TNF\alpha^+$: 7.2 ± 2.1%) (Figure S1H).

As further validation of the cytotoxic $CD4^+$ T cell phenotype in tissue, multiplex immunofluorescence tissue staining of bladder tumor tissue from a patient in the scRNA-seq data set demonstrated $CD4^+$ T cells that also express *GZMB* or *GZMK* (Figure 4F, top row; tissue staining from an additional patient in Figure S1I), at levels not seen with negative control staining (Figure 4F, bottom row).

Overall annotation of clusters from the scRNA-seq data was supported by an independent analysis that assigns each single cell to the best-known published immune subset profiled by bulk expression analysis after sorting (SingleR) (Aran et al., 2019). This corroborated the identification of Tregs (90% and 78% of $CD4_{IL2RAHI}$ and $CD4_{IL2RALO}$ cells are assigned to T regulatory cell annotations respectively), and further demonstrated that both cytotoxic $CD4^+$ states are most similar to $CD8^+$ effector memory T cells (37% and 45% of $CD4_{GZMB}$ and $CD4_{GZMK}$ cells, respectively, are assigned to effector memory $CD8^+$ cell annotations),

reinforcing their cytotoxicity profile (Figure S2F). Finally, an internal comparison of the transcriptional profiles from $CD4^+$ and $CD8^+$ TIL clusters from our scRNA-seq data indicated that while most $CD4^+$ clusters are most similar to other $CD4^+$ clusters, cytotoxic $CD4^+$ T cells are an exception. The $CD4_{GZMB}$ cytotoxic cells were most correlated with tumor-specific $CD8_{ENTPD1}$ cells (R = 0.92), while the $CD4_{GZMK}$ cytotoxic cells are most correlated with $CD8_{CM}$ and $CD8_{NAIVE}$ cells (R = 0.98 for both) (Figure S2G). The tumor-specific gene expression program of these cytotoxic $CD4^+$ cells were marked by heat shock protein expression in both states, as well as tumor overexpression of *CXCL13* and numerous immune checkpoints (*TNFRSF18/LAG3/TIGIT/HAVCR2*) as well as *ENTPD1* within $CD4_{GZMB}$ cells (Figure S2C, Table S2).

Cytotoxic $CD4^+$ T cells were enriched and clonally expanded in bladder tumors.

Of the 2 cytotoxic $CD4^+$ states, $CD4_{GZMK}$ cells were significantly enriched in abundance in tumor ($CD4_{GZMK}$ in tumor versus non-malignant tissues: 7.2 ± 0.5% versus 5.0 ± 0.5%, exact permutation test, P = 0.01, Figure 2E). Overall the $CD4^+$ compartment exhibited a bias towards regulatory over cytotoxic $CD4^+$ T cells in tumor (regulatory $CD4^+$/cytotoxic $CD4^+$ ratio = 1.8 ± 0.2) compared to non-malignant tissues where proportions of regulatory and cytotoxic $CD4^+$ T cells were more balanced (regulatory $CD4^+$/cytotoxic $CD4^+$ ratio = 1.1 ± 0.2, T-test, P = 0.04, Figure 4G). Cytotoxic $CD4^+$ T cell states contributed to the intratumoral $CD4^+$ repertoire restriction. Both cytotoxic $CD4^+$ T cell states have significantly increased Gini coefficients in tumor compared to non-malignant tissues, with $CD4_{GZMB}$ representing the more restricted cytotoxic state in tumor ($CD4_{GZMB}$: $Gini_{tumor}$ 0.21 vs $Gini_{normal}$ 0.06; $CD4_{GZMK}$: $Gini_{tumor}$ 0.12 vs $Gini_{normal}$ 0; exact permutation test, P = 0.04 for $CD4_{GZMB}$ and P = 0.002 for $CD4_{GZMK}$, Figure 4H). Hence, unbiased dscRNA-seq revealed that heterogeneous cytotoxic $CD4^+$ T cells, a subset of which are closely related to conventional cytotoxic $CD8^+$ based on their functional program, are an unexpected but frequent constituent of the bladder tumor microenvironment, some of which are quantitatively enriched in tumor. The tumor-specific clonal expansion of both cytotoxic $CD4^+$ states suggests that their restricted repertoire may result from recognition of MHCII cognate antigens that may include bladder tumor antigens.

Cytotoxic $CD4^+$ T cells possessed lytic capacity against autologous tumor cells that was restricted by autologous Tregs.

To validate the functional relevance of cytotoxic $CD4^+$ in bladder tumors, we isolated $CD4^+$ TILs by FACS, and then cultured the cells *ex vivo* with IL-2. We then co-cultured these cells with autologous tumor cells in an imaging-based time-lapse cytotoxicity assay, assessing for cell death with Annexin V. We found that expanded $CD4^+$ TIL were cytotoxic and could trigger increased tumor apoptosis ("$CD4_{total}$:tumor", Figure 4I, left panel). However, when we performed the same co-cultures, but with $CD4^+$ TIL from the same patient that were depleted of Tregs, we found that killing was increased ("$CD4_{eff}$:tumor", Figure 4I, left panel), indicating that autologous Tregs can inhibit the activity of cytotoxic $CD4^+$ T cells. Significant tumor death was seen in co-cultures with $CD4_{eff}$ TIL compared to tumor alone (Figure 4I, left panel, representative of 3 independent experiments from different patients). Furthermore, the cytotoxic activity of $CD4_{eff}$ was at least partially dependent upon MHCII recognition, as tumor apoptosis was inhibited with pre-incubation with a pan-anti-MHCII

antibody that was not seen with an isotype control antibody (Figure 4I, right panel, representative of 2 independent patients). Independent experiments with an alternative death indicator (Cytotox Red) confirmed increased autologous tumor killing with tumor/$CD4_{eff}$ co-cultures (Figure S4A), MHCII dependence of $CD4_{eff}$ killing (Figure S4B), as well as similar MHCI-dependent autologous tumor killing with expanded $CD8^+$ T cells (Figure S4C–D). Hence, flow cytometry and functional analyses from multiple independent patients confirm not only that cytotoxic $CD4^+$ T cells expressed cytolytic proteins such as granzymes and perforin in tumor tissue, but that these cells can recognize bladder tumor antigens in an MHCII-dependent fashion and were functionally competent to lyse autologous tumor cells in a manner that can be suppressed by autologous Tregs.

Proliferating $CD4^+$ T cells contained both regulatory and cytotoxic cells.

Induction of proliferating T cells can be beneficial for anti-tumor immune responses. Proliferating $CD4^+$ T cells are rapidly induced in the periphery within weeks of initiating checkpoint blockade in prostate cancer patients (Kavanaugh et al., 2008), and in separate cohorts of thymic epithelial tumors and non-small cell lung cancer treated with anti-PD-1, a higher fold change in $Ki67^+$ cells among PD-1^+ $CD8^+$ T cells in the periphery after a week was predictive of durable clinical benefit, progression-free survival, and (in the NSCLC cohorts) overall survival (Kim et al., 2019). Within our tumor-infiltrating $CD4^+$ T cell compartment in TCC, we also identified proliferating cells ($CD4_{PROLIF}$) expressing *MKI67*, microtubule-associated markers (e.g. *STMN1*/*TUBB*), and DNA-binding proteins associated with cell cycle progression such as *PCNA, HMGB1*, and *HMGB2*, which were expressed at lower levels in regulatory and cytotoxic $CD4^+$ T cells ($CD4_{PROLIF}$: $\log_2(FC) > 2.1$, Figure 2C, Table S2). A similar signature was also seen in the $CD8^+$ compartment ($CD8_{PROLIF}$, Figure 1C, Table S2). Higher resolution clustering revealed that this proliferating state is comprised of discrete groups of cells co-expressing either regulatory or cytotoxic genes, but not both simultaneously (Figure 5A). Flow cytometric analysis of separate TCC samples confirmed the presence of discrete regulatory or cytotoxic populations of $Ki67^+$ $CD4^+$ T cells that co-express either CD25, GZMB, or GZMK (Figure 5B); across multiple independent samples; 4.7 ± 1.0% (mean ± s.e.m.) of $CD4^+$ $FOXP3^+$ cells co-expressed Ki67 and CD25, while 1.2 ± 0.5% of $CD4^+$ $FOXP3^-$ $CCR7^-$ cells co-expressed Ki67 and GZMB, and 1.0 ± 0.1% of $CD4^+$ $FOXP3^-$ $CCR7^-$ cells co-expressed Ki67 and GZMK (N = 7 tumors, Figure S1J). Proliferating $Ki67^+$ $GZMB^+$ cells are also seen within the $CD8^+$ compartment of TCC patients using flow cytometry (Figure S1K). Examination of exact TCR clonotype sharing of the most expanded $CD4_{PROLIF}$ clones identified sharing with both regulatory and cytotoxic $CD4^+$ T cells, further underscoring the contribution of each state to $CD4_{PROLIF}$ cells (Figure 5C).

Given that both regulatory and cytotoxic $CD4^+$ T cells were heterogenous and composed of cells that were proliferating to a different extent, existing clusters may fail to resolve the separate contribution of specific expression programs from subsets with different proliferative capacity. Hence, we used pseudotime analysis to separate regulatory and cytotoxic cells into proliferating and non-proliferating components (Qiu et al., 2017). This analysis divided $CD4_{PROLIF}$ cells into two groups, each lying along a branch specific for either proliferating regulatory or cytotoxic $CD4^+$ T cells, with separate branches for non-

proliferating regulatory and cytotoxic cells (Figure 5D). This underscored that both regulatory and cytotoxic $CD4^+$ T cells consist of distinct proliferating and non-proliferating states in TCC, based on both transcriptomic and clonotypic analyses.

A signature of cytotoxic $CD4^+$ T cells predicts clinical response to anti-PD-L1.

To assess the importance of the specific proliferating and non-proliferating cytotoxic $CD4^+$ T cell states for patient outcomes, we performed branched expression analysis modeling (BEAM) to identify all genes that were differentially expressed between branches at branch point 1 of the pseudotime trajectory. This branch point divided proliferating cytotoxic $CD4^+$ T cells, non-proliferating cytotoxic $CD4^+$ T cells, and all other regulatory cells (Figure 5D, right panel). Hierarchical clustering identified genes upregulated preferentially in the proliferating cytotoxic branch (cluster 7), or the non-proliferating cytotoxic branch (cluster 4), but not in regulatory branches within this analysis (all genes with $q < 0.05$, heatmap of clusters and branches in Figure 5E, branch-specific signatures in Table S5). We developed a gene signature from this analysis consisting of genes that were upregulated specifically in proliferating or non-proliferating cytotoxic $CD4^+$ T cells (from cluster 7: *ABCB1*; from cluster 4: *APBA2*, *SLAMF7*, *GPR18*, *PEG10*; Figure 5E), but were not upregulated in any of the $CD8^+$ T cell states from our scRNA-seq analysis (Table S2). We then tested this gene signature's ability to predict treatment response using bulk RNA-seq data from pre-treatment tumors from a separate phase 2 trial of atezolizumab for metastatic bladder cancer (IMvigor210 [Mariathasan et al., 2018]). In 244 metastatic bladder cancer patients with pre-treatment RNA-seq data, IHC information on immune phenotype (immune desert, immune excluded, or inflamed), and information on clinical response, this gene signature was significantly correlated with clinical response to anti-PD-L1 therapy in inflamed samples ($P = 0.037$, two-tailed T test, $N = 62$ inflamed samples, Figure 5F), which was not seen in samples with an immune excluded or immune desert phenotype. Hence, we used a composite signature containing genes that discriminated proliferating and non-proliferating cytotoxic $CD4^+$ T cells to assess the specific contributions of these discrete states and found that this signature is associated with response to PD-1 blockade in a large cohort of TCC patients. This result highlights the clinical importance of possessing intratumoral cytotoxic $CD4^+$ T cell activity in response to anti-PD-L1 treatment.

Discussion

Current efforts to dissect the mechanism of tumor immune surveillance and enhance efficacy of cancer immunotherapies have primarily focused on conventional cytotoxic $CD8^+$ T cell-mediated response. However, given the known functional diversity of $CD4^+$ T cell effector responses, and emerging data that $CD4^+$ T cell recognition may be important for anti-tumor responses for instance in the context of a neoantigen vaccine (Ott et al., 2017; Sahin et al., 2017), the role of specific $CD4^+$ states in enhancing or suppressing immune responses in the tumor microenvironment, and how these are modulated by systemic therapies including immunotherapy, remain unknown. Here we use unbiased massively parallel genotypic and phenotypic profiling of the T cell compartment in localized bladder tumors and the adjacent non-malignant compartment, including those treated with anti-PD-L1 immunotherapy, as a tool to finely dissect heterogeneity in l $CD4^+$ T cell subsets. We thereby identified specific

$CD4^+$ T cell states with functional relevance for response to immunotherapy and clinical outcomes. We not only confirm the presence of $CD4^+$ T cell states with known contributions to anti-tumor immune responses, such as *CXCL13*$^+$ $CD4^+$ T cells (Schmidt et al., 2018; Gu-Trantien et al., 2013; Gu-Trantien et al., 2017; Wei et al., 2018; Zhang et al., 2018) as well as Th17 cells (Kryczek et al., 2011), we also uncover insights into the contribution of $CD4^+$ TIL to tumor control by the immune system in bladder cancer.

First, we identified distinct states of Tregs, which differed based on level of expression of *IL2RA* and immune checkpoints such as *TNFRSF18*, which is confirmed at the protein level. These Tregs possessed a private repertoire with no detected clonotype sharing with other T cell states, which would suggest that these are not induced Tregs. Since a gene signature from checkpoint-high Tregs is associated with worse outcome in non-small cell lung cancer (Guo et al., 2018), it is possible that these regulatory cells are responsible for setting a basal state of more potent immunosuppression and adverse outcomes in TCC.

Second, we identified heterogenous states of cytotoxic $CD4^+$ T cells, which were unexpected and differed in their expression of canonical cytolytic effector molecules (GZMB and GZMK, PRF1/perforin) as well as other granule-associated proteins (GNLY/granulysin, NKG7) which may have roles in target cell killing. These were distinct populations based on both scRNA-seq and orthogonal validation by flow cytometry and multiplex immunofluorescence tissue staining. Our annotation using SingleR indicated that effector states such as cytotoxic $CD4^+$ T cells found in the tumor microenvironment may not yet be annotated, and based on “best-fit” comparisons to external reference data and transcriptional correlation within our own data these cells were in fact most similar to conventional effector memory cytotoxic $CD8^+$ T cells. The functional similarity between cytotoxic $CD4^+$ T cells and conventional $CD8^+$ T cells was underscored by our finding that the $CD4_{GZMB}$ TIL were actually most similar to tumor-specific $CD8_{ENTPD1}$ cells (Duhen et al., 2018) based on transcriptional data, while the $CD4_{GZMK}$ TIL were most similar to $CD8_{CM}$ and $CD8_{NAIVE}$ cells. Although these were distinct cell types based on separate CD4 and CD8 co-receptor expression, this may indicate shared modes of tumor recognition and tumor clearance by cytotoxic $CD4^+$ and $CD8^+$ T cells. While cytotoxic $CD4^+$ T cells are present in non-small cell lung and hepatocellular carcinoma (Zheng et al., 2017a; Guo et al., 2018), circulate with ipilimumab treatment in metastatic melanoma (Kitano et al., 2013), and also are present in an infectious context where they represent a clonally expanded dengue virus-specific effector subset (Patil et al., 2018), the extent of their heterogeneity in other solid tumors (including bladder cancer), and whether these cells are important for systemic immunotherapy have remained unclear prior to this work. We found that cytotoxic $CD4^+$ subsets in bladder tumors were clonally expanded, which may be the result of recognition of cognate bladder tumor antigens. Their functional importance was confirmed by their ability to kill autologous tumor *ex vivo*. The mechanism by which these cells kill target tumor cells involves contact-dependent mechanisms based on inhibition of killing by anti-MHCII antibodies, although other mechanisms may also contribute. We have documented that these cytotoxic $CD4^+$ T cells are polyfunctional and secrete multiple cytokines such as TNFα and IFNγ, the latter which may contribute to tumor death as well through ferroptosis (Wang et al., 2019) in addition to contact-dependent cytotoxicity. Of note, apart from the subset of cells which co-express TNFα, IFNγ, and PDCD1/LAG3/

HAVCR2, cytotoxic $CD4^+$ T cells are found to generally lack surface expression of many immune checkpoints currently being tested with therapeutic antibodies in pre-clinical and clinical testing, suggesting that these effector cells may have distinct requirements for activation.

Importantly, a gene signature derived from single cell analysis of proliferating and non-proliferating cytotoxic $CD4^+$ T cells is predictive of response to anti-PD-L1 therapy in a separate set of 62 patients with inflamed metastatic bladder cancer. Most of these genes have been previously implicated in the biology of either cytotoxic effector cells or specific human $CD4^+$ T cell responses in pathogenesis or autoimmunity, including human cytotoxic $CD4^+$ T cells (Arlehamn et al., 2014; Burel et al., 2018; Campbell et al., 2018, Imbeault et al., 2012; Mattoo et al., 2016; Sumida et al., 2018; Wang et al., 2014). Overall the predictive value of this cytotoxic $CD4^+$ T cell-specific signature in a large cohort of anti-PD-L1-treated metastatic TCC patients highlights how anti-PD-L1 therapy may alter the immune microenvironment to favor activation of cytotoxic $CD4^+$ effectors, particularly in patients with pre-existing cytotoxic $CD4^+$ T cell activity.

The importance of the relative balance between regulatory and effector T cells is well-known for conventional effectors, as the regulatory $CD4^+$:cytotoxic $CD8^+$ ratio has been associated with improved survival or response to therapy in several cancers including bladder (Preston et al., 2013; Sato et al., 2005; Baras et al., 2016; Takada et al., 2018). This work identifies the biological importance of another axis involving the relative balance of regulatory T cells and these cytotoxic $CD4^+$ effectors for anti-tumor activity: removal of regulatory T cells enhanced tumor killing by cytotoxic $CD4^+$ T cells. Our findings suggest that manipulating the balance between cytotoxic $CD4^+$ and regulatory T cell states can lead to therapeutic benefit in TCC.

Finally, the origin of cytotoxic $CD4^+$ T cell effectors within tumor remains unclear. We do not find direct evidence for plasticity or interconversion of regulatory T cells into cytotoxic $CD4^+$ T cells, based on clonotype sharing. Cytotoxic $CD4^+$ T cells do share clones with the proliferating $CD4^+$ state, raising the possibility that these cells may arise from activation of other $CD4^+$ subsets, whether within the tumor milieu itself, or as the result of tumor homing of precursors which are first activated outside of the tumor in the peripheral circulation.

There are important limitations to the interpretation of this study. The size of the sample set used for single-cell discovery of T cell heterogeneity was limited to 7 patients, hence larger scale single-cell sequencing efforts in bladder cancer will help to validate these findings. The treatments administered before collection were also heterogeneous; as a result, given the limitations in sample size, our ability to directly assess modulation of T cell subsets such as cytotoxic $CD4^+$ T cells by immunotherapy in this data set is limited. Finally, the scope of our findings in this data set are limited to patients with muscle-invasive bladder cancer; further efforts will be needed to assess immune context in other bladder cancer disease states. Nonetheless, the robustness of our findings across the individual patients in this data set highlight conserved $CD4^+$ heterogeneity across patients, which is important for immune recognition of bladder tumors.

Hence this work lays an important conceptual foundation for efforts to enhance bladder tumor immunotherapy. We identify cytotoxic $CD4^+$ effectors whose distinct expression of cytolytic molecules and other marker genes will lead to further efforts to isolate and enhance activity of specific cytotoxic subsets, as well as to discover the bladder tumor antigens they are recognizing. At the same time, this work points to specific regulatory T cell states which may be more suppressive in bladder cancer and therefore represent ideal targets for parallel approaches to inhibit their activity. Collectively, our findings point to the importance of understanding multiple axes that balance suppressive regulatory T cell activity with effector function of anti-tumor immune subsets in TCC, in order to enhance our ability to effectively manipulate these with therapeutic approaches to enhance tumor control.

STAR Methods

RESOURCE AVAILABILITY

Lead Contact: Further information and requests for resources and reagents should be directed to and will be fulfilled by the Lead Contact, Lawrence Fong (lawrence.fong@ucsf.edu).

Materials Availability: Primer sequences for TCR sequencing are enumerated in Table S3. All unique reagents generated in this study are available from the Lead Contact upon request.

Data and Code Availability: Processed single-cell RNA sequencing and TCR sequencing data that support this study have been deposited in the NCBI GEO database under accession GSE149652. Raw sequencing data will be deposited in dbGaP. All software algorithms used for analysis are available for download from public repositories which are listed in the Key Resources Table.

EXPERIMENTAL MODEL AND SUBJECT DETAILS

Tissues were obtained from patients with localized bladder transitional cell carcinoma (TCC) who either received 1–2 doses of neoadjuvant atezolizumab as part of an ongoing clinical trial (UCSF IRB# 14–15423, patients were accrued sequentially to receive increasing numbers of atezolizumab doses), or standard of care treatments recommended by their treating physician including chemotherapy (gemcitabine/carboplatin) or no systemic therapy prior to planned cystectomy (these patients were consented for tissue collection under a separate protocol, UCSF IRB# 10–04057). All studies with patients and patient samples were conducted with appropriate institutional IRB approval and oversight. Patient demographics, including age, gender, disease state (all were localized muscle-invasive bladder cancer), neoadjuvant treatment, and presence of tumor and pathologic staging at the time of surgery are provided in Table S1. No formal sample size calculations were conducted for this particular collection.

METHOD DETAILS

Tissue processing—Tissues were obtained from patients with localized bladder transitional cell carcinoma (TCC) who either received neoadjuvant atezolizumab, standard

of care chemotherapy (gemcitabine/carboplatin), or no systemic therapy as per standard of care prior to planned cystectomy. Cystectomy surgical specimens were obtained fresh from the operating field, and dissected in surgical pathology where grossly apparent tumor or adjacent bladder not grossly affected by tumor ("non-malignant") were isolated, minced, and transported at room temperature immersed in L15 media with 15 mM HEPES and 600 mg% glucose. Once received, these were digested using Liberase TL as well as mechanical dissocation with heat (gentleMACS) using standard protocols. Single cell suspensions were obtained and counted for viability before staining for FACS. Healthy donor blood was separately collected, processed by gradient centrifugation to peripheral blood mononuclear cells (PBMCs), and cryopreserved to be thawed later for control experiments.

Flow cytometry/FACS—Freshly dissociated TILs and previously frozen healthy donor PBMCs were used for sorting. Samples were stained with designated panels for 30 minutes at 4°C and washed twice with FACS buffer (PBS, 2% FBS, 1mM EDTA). Cells were incubated with Draq7 (Biolegend, Cat# 424001) for 5 mins at room temperature to stain dead cells. Samples were sorted on a FACSAria Fusion (Becton Dickinson) using FACSDiva software with single channel compensation controls acquired on the same day.

For RNA sequencing flow validation, previously frozen TILs were thawed into in complete media (RPMI, 10% heat inactivated FBS, 1% non-essential amino acids solution, 10 uM HEPES, 1mM sodium pyruvate, 2 mM L-glutamine, 100 U/ml penicillin-streptomycin) and washed once with PBS. Live/dead fixable Near-IR dead cell stain (Invitrogen, Cat# L34975) was incubated with cells for 30 minutes at room temperature and washed once with FACS buffer. Samples were stained with designated panels for 30 minutes at 4°C and washed twice with FACS buffer. Cells requiring intracellular staining were fixed and permeabilized with eBioscience FoxP3/Transcription factor staining buffer set (Cat# 00-5523-00) according to the manufacturer's protocol. Intracellular staining with antibodies was carried out for 30 minutes at room temperature and washed twice with FACS wash. Cells were fixed with FluoroFix buffer (Biolegend, Cat# 422101) and washed once with FACS buffer. Cells were acquired the next day on a FACSymphony (Becton Dickinson) using FACSDiva with single channel compensation controls acquired on the same day. Data was analyzed off-line using FlowJo analysis software (FlowJo, LLC).

For cytokine expression, cells were resuspended in complete media and divided into two T25 flasks. One flask was activated with cell stimulation cocktail (eBioscience, cat# 00–4975 containing phorbol 12-myristate 13-acetate, ionomycin, brefeldin A and monensin at a final concentration of 81 nM, 1.34 nM, 10.6 μM and 2 μM respectively) and both flasks were incubated upright for 3 h in a CO_2 incubator at 37°C. Cells were collected and washed once with PBS prior to Live/Dead Fixable Near-IR dead cell staining and surface and intracellular flow staining as described above.

Antibodies used for sorting were Brilliant Violet 605 CD25 (Biolegend, clone BC96, Cat# 302632), Brilliant Violet 786 CD127 (Biolegend, clone A019D5, Cat# 351330), Brilliant Violet 421 CD4 (Biolegend, clone OKT4, Cat# 317434), Brilliant Violet 650 CD3 (Biolegend, clone UCHT1, Cat# 300468), Brilliant Ultraviolet 395 CD45 (Becton Dickinson, clone H130, Cat# 563792), and Alexa Fluor 647 CD8 (Biolegend, clone SK1,

Cat# 344726). Antibodies used for RNA sequencing flow validation were FITC GZMK (Biolegend, clone GM26E7, Cat# 370508), PerCP-Cy5.5 HLA-DR (Biolegend, clone L243, Cat# 307630), APC-R700 CCR7 (Becton Dickinson, clone 3D12, Cat# 565867), Brilliant Violet 480 CD3 (Becton Dickinson, clone UCHT1, Cat# 566105), Brilliant Violet 510 GZMB (Becton Dickinson, clone GB11, Cat# 563388), Brilliant Violet 605 Ki67 (Biolegend, clone Ki-67, Cat# 350522), Brilliant Violet 650 CD45RA (Biolegend, clone HI100, Cat# 304136), Brilliant Violet 786 CD25 (Biolegend, clone BC96, Cat# 302638), Brilliant violet 711 TNFSRF18 (Biolegend, clone 108–17, Cat# 371212), Brilliant ultraviolet 395 CD4 (Becton Dickinson, clone RPA-T4, Cat# 564724), Brilliant ultraviolet 496 CD8 (Becton Dickinson, clone RPA-T8, Cat# 564808), Brilliant ultraviolet 805 CD45 (Becton Dickinson, clone HI30, Cat# 564914), PE-CF594 FoxP3 (Becton Dickinson, clone 259D/C7), PE-Cy7 Perforin (Biolegend, clone B-D48, Cat# 353316).

Antibodies used for cytokine staining in addition to those used above were Alexa Fluor 647 IFNγ (Biolegend, clone 4S.B3, Cat# 502516) and PE anti-human TNFα (Biolegend, clone Mab11, Cat# 502909).

Single cell RNA sequencing—Droplet-based single-cell RNA sequencing (dscRNA-seq) was performed using the 10X Genomics Chromium Single Cell 3’ platform, version 1, according to manufacturer’s instructions. $CD3^+CD4^+$ and $CD3^+CD8^+$ T cells were sorted from digested tumor and non-malignant tissues, or Ficoll-purified and previously cryopreserved healthy control PBMCs, into 500 ul of PSA/0.04% BSA for loading onto 10X. Following library preparation, sequencing was performed on an Illumina HiSeq 2500 (Rapid Run mode). Paired samples from the same experiment and patient were processed in parallel during library preparation, and sequenced on the same flowcell to minimize batch effects.

TCR sequencing—In brief, approximately 10% of the barcoded cDNA from the 10X workflow was utilized for TCR analysis. Primers used for TCR sequencing are listed in Table S3. cDNA were first amplified with 6–12 amplification cycles using a template switching oligonucleotide (TSO) and P7 primers. A pool of forward Vα and Vβ primers containing the TruSeq Read 1 primer sequence were then used in conjunction with a reverse P7 primer to amplify CDR3 sequences from the TCR alpha and beta loci. An additional amplification step using forward primers containing the Illumina P5, i5 and Truseq Read 1 sequences was used with reverse P7 primer to create final TCR libraries for sequencing. Deep sequencing was done on an Illumina NovaSeq S1 with separate lanes for the TCR alpha and TCR beta sequencing. Read 1 contained 280 bp of the TCR alpha or beta CDR3 sequence, and the i7 read contained the 14 bp 10X barcode.

Expression analysis—After 10X sequencing data was processed through the Cell Ranger pipeline (version 1.1) with default settings, filtered gene-barcode matrices for single tumors were analyzed using the scanpy toolkit (Wolf et al. 2018). Genes that were detected in less than three cells were filtered out, and cells were filtered out with greater than ten percent of mitochondrial genes and with fewer than 100 or greater than 1200 detected genes. Cells that were annotated as red blood cells (HBB) or macrophage (CD14, CD68, CD163) were also excluded from downstream analyses. The gene expression values were $\log_2$ plus

one transformed and normalized to 10,000 counts per cell. The resulting matrix was batch corrected by regressing out total UMI counts and percent mitochondrial genes using the built-in scanpy function followed by using the scanpy implementation of ComBat (Johnson et al., 2007) with each well acting as a batch (13 wells total). The adjusted matrix was scaled to a mean of zero and variance of 1. Highly variable genes were selected using the embedded scanpy function followed by principal component analysis (PCA), leiden clustering and UMAP plotting with default settings with the exception of using a resolution of 1.5 for $CD4^+$ T cells and 1.0 for $CD8^+$ T cells for the leiden clustering. This yielded 18 clusters which were collapsed to 11 cell types based on manual gene annotations (for $CD4^+$ cells), and 11 clusters (for $CD8^+$ cells). We performed differential expression to identify marker genes that were upregulated in each individual cluster relative to the combination of all other single cells (regardless of tumor or non-malignant tissue origin), or genes that were upregulated in tumor versus non-malignant compartments. We compared the gene lists to known literature to label the clusters, as well as using SingleR (Aran et al., 2019) to map the expression signature for each cluster to the best correlated candidate immune reference signature, using the Monaco bulk RNA-seq reference of sorted human immune cell populations described within (Monaco et al., 2019). Significant differences between the cell type abundances for the normal and tumor tissue samples were assessed using an exact permutation test on the abundances.

Correlation analysis between gene expression from distinct clusters was performed by restricting to genes expressed across all clusters being tested, and then correlating the scaled expression of the multidimensional vector of shared genes between pairs of clusters.

TCR analysis—TRA and TRB CDR3 nucleotide reads were demultiplexed by matching reads to 10X barcodes from cells with existing expression data that passed filtering in the Cell Ranger pipeline, excluding cell barcodes that overlapped between multiple samples. Following demultiplexing of the TRA and TRB CDR3s, reads were aligned against known TRA/TRB CDR3 sequences then assembled into clonotype families using miXCR (Bolotin et al., 2015) with similar methodologies to a previous study (Zemmour et al., 2018). For any given 10X barcode, the most abundant TRA or TRB clonotype was accepted for further analysis; if 2 TRA or TRB clonotypes were equally abundant for a given 10X barcode, the clonotype with the highest sequence alignment score was used for further analysis. Detailed sequencing statistics and saturation analysis are provided in Table S3. Only cells with paired TRA and TRB were used for further downstream analysis. Analysis utilizing TCR data only (number of unique cells sharing a specific TRA/TRB clonotype sequence, Gini coefficient) utilized cells both with and without a specific functional population that had been assigned by clustering. Analysis involving both TCR clonotype and function was restricted to cells with both a mapped TRA/TRB and a functional population from clustering. Statistical comparisons of Gini coefficients across compartments was performed using Wilcoxon signed-rank test with Benjamini-Hochberg correction for multiple testing; statistical testing of differences in Gini coefficients between tumor and non-malignant compartments across all phenotypic clusters was performed using exact permutation testing.

Tumor infiltrating lymphocyte (TIL) isolation and culturing—Single-cell suspensions from processed and digested bladder tumors were viably frozen at −80 C and stored prior to culture setup. To sort the tumor-infiltrating lymphocytes, frozen cancer cell aliquots were thawed, washed once with PBS, and counted by Vicell. Cells were subsequent stained and sorted by FACS. CD4 TIL ($Draq7^{-}CD45^{+}CD3^{+}CD4^{+}$ that were not $CD25^{+}CD127^{lo}$) and CD8 TIL ($Draq7^{-}CD45^{+}CD3^{+}CD8^{+}$) were sorted into ImmunoCult XF complete medium (Medium + 10% FCS + 1% penicillin/streptomycin; STEMCELL Technologies #10981). T cells were pooled together for culturing. After centrifugation, T cells were suspended in ImmunoCult XF complete medium, and Dynabeads Human T-Activator CD3/CD28/CD137 (Gibco #11162D) were added to the culture per manufacturer's protocol. T cells were cultured in 96 well U-bottom plates, and briefly centrifuged to ensure cell contact with Dynabeads. T cell expansion was managed in two phases. For the first week of T cell expansion, TILs were maintained with ImmunoCult XF complete medium + 200 IU/ml of human recombinant IL-2 (Peprotech #200–02). From the second week onward, IL-2 concentration was gradually increased from 200 IU/ml to 2000 IU/ml based on cell growth kinetics (which varied by patient sample). T cells were harvested between 5–8 weeks for functional killing assays.

Cytotoxic T lymphocyte (CTL) killing assay—After expansion, TILs were again sorted for either CD4 or CD8 as distinct effector populations. Primary cancer cells from frozen aliquots were freshly thawed and sorted on $CD45^{-}Draq7^{-}$ as target cells. To achieve various effector-to-target (E:T) ratios, 3000 cancer cell targets were suspended in ImmunoCult XF complete medium and seeded into each well. Different ratios of TILs were serially diluted and added to the corresponding wells. Each well contained 200 μl of medium supplemented with 1 μl/well of IncuCyte Annexin V Red reagent (Essen Bioscience #4641). For MHCI and MHCII blockade, 10 μg of blocking antibody (or isotype control matched to the anti-MHCII antibody) was added into wells containing cancer cells and cultured at 37 C for 1 hour prior to co-culture with TILs. Cell culture was monitored by the IncuCyte Zoom system (Essen Bioscience) at 15–30 minute intervals for up to 36 h when needed. Experiments with Annexin V were carried out with samples from 3 independent patients. Additional experiments were performed using 0.25 μl of IncuCyte Cytotox Red reagent (Essen Bioscience #4632) instead of Annexin V; 2 independent experiments were performed with Cytotox Red using distinct aliquots from the same patient. Analysis was performed using the IncuCyte Zoom software, using images background subtracted with a tophat filter. For Annexin V experiments, background death was subtracted, with all traces displayed as relative change in cell death from timepoint 0. For Cytotox Red experiments, tumor cells were larger than TIL based on inspection of wells with tumor cells alone or free TILs in wells containing TILs; based on this, the number of dying tumor cells per mm^2 was determined using a minimum area threshold of 75 μm^2. Out of focus frames were discarded, as were any wells where the first timeframe was out of focus precluding accurate normalization.

Pseudotime analysis—Pseudotime analysis, including branched expression analysis modeling (BEAM) to identify all genes with branch-dependent differential expression followed by unbiased clustering of genes based on patterns of co-expression in specific

branches, was performed using Monocle v2.10.1 as described (Qiu et al., 2017), for the combination of proliferating ($CD4_{PROLIF}$, regulatory ($CD4_{IL2RAHI}$, $CD4_{IL2RALO}$) and cytotoxic ($CD4_{GZMB}$, $CD4_{GZMK}$) states from scRNA-seq clustering.

Gene signature analysis—Genes were selected based on their specific upregulation in proliferating or non-proliferating cytotoxic $CD4^+$ T cell branches, but not in regulatory T cell branches, from the pseudotime analysis. Genes that overlapped with differentially expressed genes in any of the $CD8^+$ T cell states from our scRNA-seq analysis (Table S2) were removed. The resulting gene list was used to construct a composite signature consisting of genes that distinguish either proliferating or non-proliferating cytotoxic $CD4^+$ T cells; a signature score was computed as previously published for the IMvigor210 data set (Mariathasan et al., 2018), by z-score transforming the expression of each gene in the signature, and then using the first component (PC1) of a principal component analysis as the gene signature score. Immune subtypes for the IMvigor210 samples for this analysis were previously assigned based on CD8 immunohistochemistry staining (Mariathasan et al., 2018).

RNAscope/tissue immunofluorescence staining—RNAscope (Advanced Cell Diagnostics) *in situ* hybridization and immunofluorescence staining were performed on 4 μm FFPE sections from cystectomy specimens with existing scRNA-seq and TCR-seq data. Tissues were pre-treated with target retrieval reagents and protease to improve target recovery based on guidelines provided in the RNAscope Multiplex Fluorescent Reagent Kit v2 Assay protocol. Probes for human *GZMB* and *GZMK* mRNA (ACD) were incubated at 1:700 dilution for 2 hr 40 min. The probe was then hybridized with Opal 7-Color Manual IHC Kit (PerkinElmer), with detection of *GZMB* and *GZMK* using Opal 620 and Opal 540 respectively. Samples were then immunofluorescence stained for human CD4 (Cell Marque) which was detected using Alexa Fluor 555-conjugated goat anti-rabbit IgG secondary antibody (Invitrogen). Tissues were counterstained with DAPI. Slides were imaged using a TCS SP8 X white light laser inverted confocal microscope (Leica Microsystems). No staining was seen with negative control probes (for RNAscope) or with secondary antibody alone (for immunofluorescence) for tumor tissue from cystectomy specimens (shown in Figure 4F) or healthy tonsil tissue (data not shown).

QUANTIFICATION AND STATISTICAL ANALYSIS

Specific statistical tests and metrics (median, mean, standard error) used for comparisons, along with sample sizes, are described in the Results and figure legends. The chemotherapy sample was included in unbiased clustering, testing for conserved marker genes and tumor vs non-malignant testing, but was excluded from analyses of treatment effect (anti-PD-L1 vs untreated).

ADDITIONAL RESOURCES

The clinical trial of neoadjuvant atezolizumab prior to planned cystectomy for localized bladder cancer is registered under clinicaltrials.gov (NCT02451423).

Supplementary Material

Refer to Web version on PubMed Central for supplementary material.

Acknowledgements

The patients who volunteered to participate in these studies; UCSF Genitourinary Medical Oncology and Urology providers involved in screening, enrollment, and clinical care of these patients; UCSF Biospecimen Resources Program for assistance with tissue acquisition; Institute for Human Genetics Core for assistance with sequencing. This work was supported by the Parker Institute for Cancer Immunotherapy. D.Y. Oh is supported by NIH T32CA177555, K08AI139375, the Harry F. Bisel, MD Endowed Young Investigator Award from the Conquer Cancer Foundation of the American Society of Clinical Oncology, the Bladder Cancer Advocacy Network Palm Beach New Discoveries Young Investigator Award, and the Prostate Cancer Foundation Young Investigator Award. S.S. Kwek is supported by the Peter Michael Foundation. L. Fong is support by the Parker Institute of Cancer Immunotherapy, the Prostate Cancer Foundation and NIH R01CA194511, R01CA223484, U01CA233100, and U01CA244452.

References

Aran D, Looney AP, Liu L, Wu E, Fong V, Hsu A, Chak S, Naikawadi RP, Wolters PJ, Abate AR, et al. (2019). Reference-based analysis of lung single-cell sequencing reveals a transitional profibrotic macrophage. Nat. Immunol 20, 163–172. [PubMed: 30643263]

Arlehamn CL, Seumois G, Gerasimova A, Huang C, Fu Z, Yue X, Sette A, Vijayanand P, and Peters B (2014). Transcriptional profile of tuberculosis antigen-specific T cells reveals novel multifunctional features. J. Immunol 193, 2931–40. [PubMed: 25092889]

Ayers M, Lunceford J, Nebozhyn M, Murphy E, Loboda A, Kaufman DR, Albright A, Cheng JD, Kang SP, Shankaran V, et al. (2017). IFN-γ-related mRNA profile predicts clinical response to PD-1 blockade. J. Clin. Invest 127, 2930–2940. [PubMed: 28650338]

Baras AS, Drake C, Liu JJ, Gandhi N, Kates M, Hoque MO, Meeker A, Hahn N, Taube JM, Schoenberg MP, et al. (2016). The ratio of CD8 to Treg tumor-infiltrating lymphocytes is associated with response to cisplatin-based neoadjuvant chemotherapy in patients with muscle invasive urothelial carcinoma of the bladder. Oncoimmunology 5, e1134412. [PubMed: 27467953]

Bolotin DA, Poslavsky S, Mitrophanov I, Shugay M, Mamedov IZ, Putintseva EV, and Chudakov DM (2015). MiXCR: software for comprehensive adaptive immunity profiling. Nat. Methods 12, 380–1. [PubMed: 25924071]

Burel JG, Lindestam Arlehamn CS, Khan N, Seumois G, Greenbaum JA, Taplitz R, Gilman RH, Saito M, Vijayanand P, Sette A, et al. (2018). Transcriptomic Analysis of CD4+ T Cells Reveals Novel Immune Signatures of Latent Tuberculosis. J. Immunol 200, 3283–3290. [PubMed: 29602771]

Büttner M, Miao Z, Wolf FA, Teichmann SA, and Theis FJ (2019). A test metric for assessing single-cell RNA-seq batch correction. Nat. Methods 16, 43–49. [PubMed: 30573817]

Campbell KS, Cohen AD, and Pazina T (2018). Mechanisms of NK Cell Activation and Clinical Activity of the Therapeutic SLAMF7 Antibody, Elotuzumab in Multiple Myeloma. Front Immunol. 9, 2551. [PubMed: 30455698]

Cancer Genome Atlas Research Network. (2008). Comprehensive genomic characterization defines human glioblastoma genes and core pathways. Nature 455, 1061–8. [PubMed: 18772890]

De Simone M, Arrigoni A, Rossetti G, Gruarin P, Ranzani V, Politano C, Bonnal RJP, Provasi E, Sarnicola ML, Panzeri I, et al. (2016). Transcriptional Landscape of Human Tissue Lymphocytes Unveils Uniqueness of Tumor-Infiltrating T Regulatory Cells. Immunity 45, 1135–1147. [PubMed: 27851914]

Duhen T, Duhen R, Montler R, Moses J, Moudgil T, de Miranda NF, Goodall CP, Blair TC, Fox BA, McDermott JE, et al. (2018). Co-expression of CD39 and CD103 identifies tumor-reactive CD8 T cells in human solid tumors. Nat. Commun 9, 2724. [PubMed: 30006565]

Hargadon KM, Johnson CE, and Williams CJ (2018). Immune checkpoint blockade therapy for cancer: An overview of FDA-approved immune checkpoint inhibitors. Int. Immunopharmacol 62, 29–39. [PubMed: 29990692]

Herbst RS, Soria JC, Kowanetz M, Fine GD, Hamid O, Gordon MS, Sosman JA, McDermott DF, Powderly JD, Gettinger SN, et al. (2014). Predictive correlates of response to the anti-PD-L1 antibody MPDL3280A in cancer patients. Nature 515, 563–7. [PubMed: 25428504]

Gu-Trantien C, Loi S, Garaud S, Equeter C, Libin M, de Wind A, Ravoet M, Le Buanec H, Sibille C, Manfouo-Foutsop G, et al. (2013). $CD4^+$ follicular helper T cell infiltration predicts breast cancer survival. J. Clin. Invest 123, 2873–92. [PubMed: 23778140]

Gu-Trantien C, Migliori E, Buisseret L, de Wind A, Brohée S, Garaud S, Noël G, Dang Chi VL, Lodewyckx JN, Naveaux C, et al. (2017). CXCL13-producing TFH cells link immune suppression and adaptive memory in human breast cancer. J. Clin. Invest. Insight 2, pii: 91487.

Guo X, Zhang Y, Zheng L, Zheng C, Song J, Zhang Q, Kang B, Liu Z, Jin L, Xing R, et al. (2018). Global characterization of T cells in non-small-cell lung cancer by single-cell sequencing. Nat. Med 24, 978–985. [PubMed: 29942094]

Hodi FS, O'Day SJ, McDermott DF, Weber RW, Sosman JA, Haanen JB, Gonzalez R, Robert C, Schadendorf D, Hassel JC, et al. (2010). Improved survival with ipilimumab in patients with metastatic melanoma. N. Engl. J. Med 363, 711–23. [PubMed: 20525992]

Imbeault M, Giguère K, Ouellet M, and Tremblay MJ (2012). Exon level transcriptomic profiling of HIV-1-infected CD4(+) T cells reveals virus-induced genes and host environment favorable for viral replication. PLoS Pathog. 8, e1002861. [PubMed: 22876188]

Johnson WE, Li C, and Rabinovic A (2007). Adjusting batch effects in microarray expression data using empirical Bayes methods. Biostatistics. 8, 118–27. [PubMed: 16632515]

Kavanagh B, O'Brien S, Lee D, Hou Y, Weinberg V, Rini B, Allison JP, Small EJ, and Fong L (2008). CTLA4 blockade expands FoxP3+ regulatory and activated effector CD4+ T cells in a dose-dependent fashion. Blood. 112, 1175–83. [PubMed: 18523152]

Kim KH, Cho J, Ku BM, Koh J, Sun JM, Lee SH, Ahn JS, Cheon J, Min YJ, Park SH, et al. (2019). The First-week Proliferative Response of Peripheral Blood PD-1+CD8+ T Cells Predicts the Response to Anti-PD-1 Therapy in Solid Tumors. Clin. Cancer Res 25, 2144–2154. [PubMed: 30647082]

Kitano S, Tsuji T, Liu C, Hirschhorn-Cymerman D, Kyi C, Mu Z, Allison JP, Gnjatic S, Yuan JD, and Wolchok JD (2013). Enhancement of tumor-reactive cytotoxic $CD4^+$ T cell responses after ipilimumab treatment in four advanced melanoma patients. Cancer Immunol. Res 1, 235–44. [PubMed: 24396833]

Koshkin VS, and Grivas P (2018). Emerging Role of Immunotherapy in Advanced Urothelial Carcinoma. Curr. Oncol. Rep 20, 48. [PubMed: 29644490]

Krensky AM, and Clayberger C (2009). Biology and clinical relevance of granulysin. Tissue Antigens 73, 193–8. [PubMed: 19254247]

Kryczek I, Zhao E, Liu Y, Wang Y, Vatan L, Szeliga W, Moyer J, Klimczak A, Lange A, and Zou W (2011). Human TH17 cells are long-lived effector memory cells. Sci. Transl. Med 3, 104ra100.

Kurioka A, Walker LJ, Klenerman P, Willberg CB (2016). MAIT cells: new guardians of the liver. Clin. Transl. Immunology 5, e98. [PubMed: 27588203]

Liakou CI, Kamat A, Tang DN, Chen H, Sun J, Troncoso P, Logothetis C, and Sharma P (2008). CTLA-4 blockade increases IFNgamma-producing CD4+ICOShi cells to shift the ratio of effector to regulatory T cells in cancer patients. Proc. Natl. Acad. Sci. U.S.A 105, 14987–9. [PubMed: 18818309]

Löfroos AB, Kadivar M, Resic Lindehammer S, and Marsal J (2017). Colorectal cancer-infiltrating T lymphocytes display a distinct chemokine receptor expression profile. Eur. J. Med. Res 22, 40. [PubMed: 29020986]

Mariathasan S, Turley SJ, Nickles D, Castiglioni A, Yuen K, Wang Y, Kadel EE III, Koeppen H, Astarita JL, Cubas R, et al. (2018). TGFβ attenuates tumour response to PD-L1 blockade by contributing to exclusion of T cells. Nature 554, 544–548. [PubMed: 29443960]

Martincorena I, and Campbell PJ (2015). Somatic mutation in cancer and normal cells. Science 349, 1483–9. [PubMed: 26404825]

Mattoo H, Mahajan VS, Maehara T, Deshpande V, Della-Torre E, Wallace ZS, Kulikova M, Drijvers JM, Daccache J, Carruthers MN, et al. (2016). Clonal expansion of CD4(+) cytotoxic T

lymphocytes in patients with IgG4-related disease. J. Allergy Clin. Immunol 138, 825–838. [PubMed: 26971690]

McInnes L, and Healy J (2018). UMAP: Uniform Manifold Approximation and Projection for Dimension Reduction. arXiv:1802.03426 [stat.ML]

Medley QG, Kedersha N, O'Brien S, Tian Q, Schlossman SF, Streuli M, and Anderson P (1996). Characterization of GMP-17, a granule membrane protein that moves to the plasma membrane of natural killer cells following target cell recognition. Proc. Natl. Acad. Sci. U.S.A 93, 685–9. [PubMed: 8570616]

Monaco G, Lee B, Xu W, Mustafah S, Hwang YY, Carré C, Burdin N, Visan L, Ceccarelli M, Poidinger M, et al. (2019). RNA-Seq Signatures Normalized by mRNA Abundance Allow Absolute Deconvolution of Human Immune Cell Types. Cell Rep. 26, 1627–1640.e7. [PubMed: 30726743]

Oldham KA, Parsonage G, Bhatt RI, Wallace DM, Deshmukh N, Chaudhri S, Adams DH, and Lee SP (2012). T lymphocyte recruitment into renal cell carcinoma tissue: a role for chemokine receptors CXCR3, CXCR6, CCR5, and CCR6. Eur. Urol 61, 385–94. [PubMed: 22079021]

Ott PA, Hu Z, Keskin DB, Shukla SA, Sun J, Bozym DJ, Zhang W, Luoma A, Giobbie-Hurder A, Peter L, et al. (2017). An immunogenic personal neoantigen vaccine for patients with melanoma. Nature 547, 217–221. [PubMed: 28678778]

Parsonage G, Machado LR, Hui JW, McLarnon A, Schmaler T, Balasothy M, To KF, Vlantis AC, van Hasselt CA, Lo KW, et al. (2012). CXCR6 and CCR5 localize T lymphocyte subsets in nasopharyngeal carcinoma. Am. J. Pathol 180, 1215–22. [PubMed: 22226739]

Patil VS, Madrigal A, Schmiedel BJ, Clarke J, O'Rourke P, de Silva AD, Harris E, Peters B, Seumois G, Weiskopf D, et al. (2018). Precursors of human $CD4^+$ cytotoxic T lymphocytes identified by single-cell transcriptome analysis. Sci. Immunol 3, pii: eaan8664.

Philip M, Fairchild L, Sun L, Horste EL, Camara S, Shakiba M, Scott AC, Viale A, Lauer P, Merghoub T, et al. (2017). Chromatin states define tumour-specific T cell dysfunction and reprogramming. Nature 545, 452–456. [PubMed: 28514453]

Plitas G, Konopacki C, Wu K, Bos PD, Morrow M, Putintseva EV, Chudakov DM, and Rudensky AY (2016). Regulatory T Cells Exhibit Distinct Features in Human Breast Cancer. Immunity 45, 1122–1134. [PubMed: 27851913]

Powles T, Eder JP, Fine GD, Braiteh FS, Loriot Y, Cruz C, Bellmunt J, Burris HA, Petrylak DP, Teng SL, et al. (2014). MPDL3280A (anti-PD-L1) treatment leads to clinical activity in metastatic bladder cancer. Nature 515, 558–62. [PubMed: 25428503]

Preston CC, Maurer MJ, Oberg AL, Visscher DW, Kalli KR, Hartmann LC, Goode EL, and Knutson KL (2013). The ratios of $CD8^+$ T cells to $CD4^+CD25^+$ $FOXP3^+$ and $FOXP3^-$ T cells correlate with poor clinical outcome in human serous ovarian cancer. PLoS One 8, e80063 [PubMed: 24244610]

Qiu X, Mao Q, Tang Y, Wang L, Chawla R, Pliner HA, and Trapnell C (2017). Reversed graph embedding resolves complex single-cell trajectories. Nat. Methods 14, 979–982. [PubMed: 28825705]

Robert C, Long GV, Brady B, Dutriaux C, Maio M, Mortier L, Hassel JC, Rutkowski P, McNeil C, Kalinka-Warzocha E, et al. (2015). Nivolumab in previously untreated melanoma without BRAF mutation. N. Engl. J. Med 372, 320–30. [PubMed: 25399552]

Sahin U, Derhovanessian E, Miller M, Kloke BP, Simon P, Löwer M, Bukur V, Tadmor AD, Luxemburger U, Schrörs B, et al. (2017). Personalized RNA mutanome vaccines mobilize poly-specific therapeutic immunity against cancer. Nature 547, 222–226. [PubMed: 28678784]

Sato E, Olson SH, Ahn J, Bundy B, Nishikawa H, Qian F, Jungbluth AA, Frosina D, Gnjatic S, Ambrosone C, et al. (2005). Intraepithelial $CD8^+$ tumor-infiltrating lymphocytes and a high $CD8^+$/regulatory T cell ratio are associated with favorable prognosis in ovarian cancer. Proc. Natl. Acad. Sci. U.S.A 102, 18538–43. [PubMed: 16344461]

Schmidt M, Weyer-Elberich V, Hengstler JG, Heimes AS, Almstedt K, Gerhold-Ay A, Lebrecht A, Battista MJ, Hasenburg A, Sahin U, et al. (2018). Prognostic impact of CD4-positive T cell subsets in early breast cancer: a study based on the FinHer trial patient population. Breast Cancer Res. 20, 15. [PubMed: 29482642]

Sumida H, and Cyster JG (2018). G-Protein Coupled Receptor 18 Contributes to Establishment of the CD8 Effector T Cell Compartment. Front. Immunol 9, 660. [PubMed: 29670628]

Takada K, Kashiwagi S, Goto W, Asano Y, Takahashi K, Takashima T, Tomita S, Ohsawa M, Hirakawa K, and Ohira M (2018). Use of the tumor-infiltrating CD8 to FOXP3 lymphocyte ratio in predicting treatment responses to combination therapy with pertuzumab, trastuzumab, and docetaxel for advanced HER2-positive breast cancer. J. Transl. Med 16, 86. [PubMed: 29615076]

Tirosh I, Izar B, Prakadan SM, Wadsworth MH 2nd, Treacy D, Trombetta JJ, Rotem A, Rodman C, Lian C, Murphy G, et al. (2016). Dissecting the multicellular ecosystem of metastatic melanoma by single-cell RNA-seq. Science 352, 189–96. [PubMed: 27124452]

Traag VA, Waltman L, and van Eck NJ (2019). From Louvain to Leiden: guaranteeing well-connected communities. Sci Rep. 9, 5233. [PubMed: 30914743]

Tumeh PC, Harview CL, Yearley JH, Shintaku IP, Taylor EJ, Robert L, Chmielowski B, Spasic M, Henry G, Ciobanu V, et al. (2014). PD-1 blockade induces responses by inhibiting adaptive immune resistance. Nature 515, 568–71. [PubMed: 25428505]

Wang W, Green M, Choi JE, Gijón M, Kennedy PD, Johnson JK, Liao P, Lang X, Kryczek I, Sell A, et al. (2019). CD8+ T cells regulate tumour ferroptosis during cancer immunotherapy. Nature. 569, 270–274. [PubMed: 31043744]

Wang X, Sumida H, and Cyster JG (2014). GPR18 is required for a normal CD8αα intestinal intraepithelial lymphocyte compartment. J. Exp. Med 211, 2351–9. [PubMed: 25348153]

Wei Y, Lin C, Li H, Xu Z, Wang J, Li R, Liu H, Zhang H, He H, and Xu J (2018). CXCL13 expression is prognostic and predictive for postoperative adjuvant chemotherapy benefit in patients with gastric cancer. Cancer Immunol. Immunother 67, 261–269. [PubMed: 29085997]

Wolf F, Angerer P, and Theis F (2018). SCANPY: large-scale single-cell gene expression data analysis. Genome Biol. 19, 15. [PubMed: 29409532]

Yao C, Sun HW, Lacey NE, Ji Y, Moseman EA, Shih HY, Heuston EF, Kirby M, Anderson S, Cheng J, et al. (2019). Single-cell RNA-seq reveals TOX as a key regulator of CD8+ T cell persistence in chronic infection. Nat. Immunol 20, 890–901. [PubMed: 31209400]

Zemmour D, Zilionis R, Kiner E, Klein AM, Mathis D, and Benoist C (2018). Single-cell gene expression reveals a landscape of regulatory T cell phenotypes shaped by the TCR. Nat. Immunol 19, 291–301. [PubMed: 29434354]

Zhang L, Yu X, Zheng L, Zhang Y, Li Y, Fang Q, Gao R, Kang B, Zhang Q, Huang JY, et al. (2018). Lineage tracking reveals dynamic relationships of T cells in colorectal cancer. Nature 564, 268–272. [PubMed: 30479382]

Zheng C, Zheng L, Yoo JK, Guo H, Zhang Y, Guo X, Kang B, Hu R, Huang JY, Zhang Q, et al. (2017a). Landscape of Infiltrating T Cells in Liver Cancer Revealed by Single-Cell Sequencing. Cell 169, 1342–1356.e16. [PubMed: 28622514]

Zheng GX, Terry JM, Belgrader P, Ryvkin P, Bent ZW, Wilson R, Ziraldo SB, Wheeler TD, McDermott GP, Zhu J, et al. (2017b). Massively parallel digital transcriptional profiling of single cells. Nat. Commun 8, 14049. [PubMed: 28091601]

Highlights (Oh et al.)

- Human bladder tumors contain multiple clonally expanded cytotoxic $CD4^+$ T cell states
- Cytotoxic $CD4^+$ T cells can kill autologous tumor in an MHCII-dependent fashion
- Autologous regulatory T cells can inhibit the activity of cytotoxic $CD4^+$ T cells
- A cytotoxic $CD4^+$ gene signature predicts response to anti-PD-L1 in bladder cancer

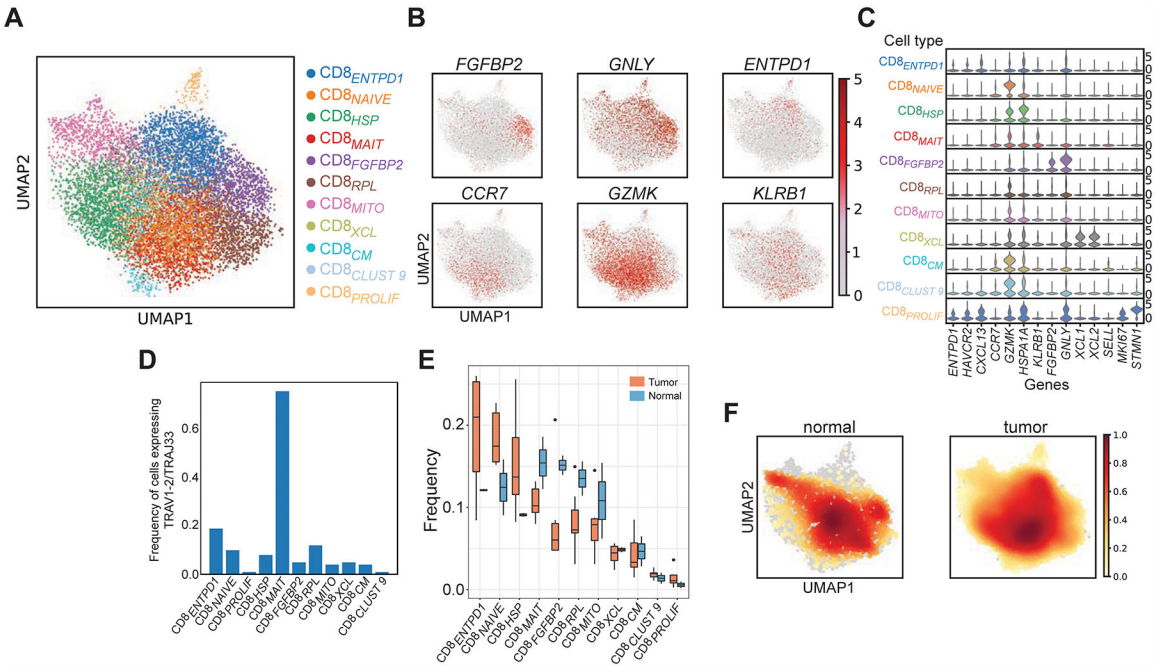

Figure 1. Bladder cancer contains canonical CD8$^+$ T cell states.

(A) Uniform Manifold Approximation and Projection (UMAP) plots of 10,762 single sorted CD3$^+$ CD8$^+$ T cells obtained from bladder tumors and adjacent non-malignant tissue are shown (N = 7 patients). Phenotypic clusters are represented in distinct colors. (B) Relative intensity of expression of select genes superimposed upon the UMAP projections in (A) are shown. (C) Violin plots show the relative expression of select differentially expressed genes (columns) for each cluster shown in (A) (rows) (all P_{adj} values < 0.05). (D) The frequency of cells expressing MAIT associated TRAV1–2/TRAJ33$^+$ TCR within each defined CD8$^+$ phenotypic cluster is shown. (E) The frequency of cells in individual clusters is shown as a proportion of total CD8$^+$ cells within either tumor or non-malignant compartments across all patients (orange = tumor, blue = non-malignant). Statistical testing was done using exact permutation test. (F) Density plots showing distribution of cells in tumor or non-malignant samples.

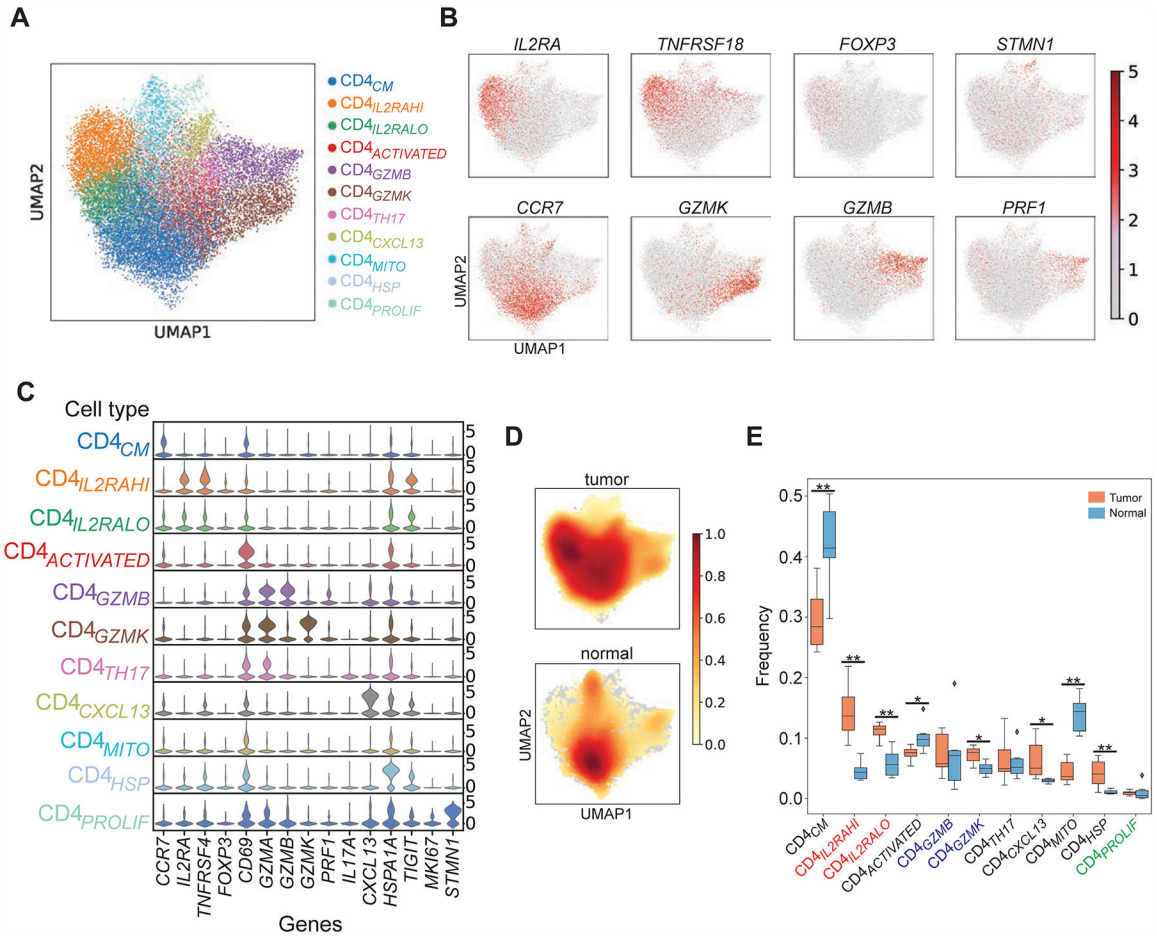

Figure 2. CD4$^+$ T cells in bladder tumors are composed of multiple distinct functional states.

(A) UMAP plots of 19,842 single sorted CD3$^+$ CD4$^+$ T cells obtained from bladder tumors and adjacent non-malignant tissue (N = 7 patients). Each distinct phenotypic cluster identified using leiden clustering is identified with a distinct color. Annotation of each unbiased cluster was performed by manual inspection of highest-ranked differentially expressed genes for each cluster, and also using reference signature-based correlation methods (SingleR) as described in the text. (B) Relative intensity of expression of select genes superimposed upon the UMAP projections shown in (A). (C) Violin plot showing relative expression of select differentially expressed genes (columns) for each cluster shown in (A) (rows) (all P_{adj} values < 0.05). (D) Density plots showing distribution of cells in tumor or non-malignant samples. (E) The frequency of cells in individual CD4$^+$ T cell states defined by scRNA-seq clustering is shown as a proportion of total CD4$^+$ cells within either tumor or non-malignant compartments across all patients (orange = tumor, blue = non-malignant). *, P < 0.05, **, P < 0.01 by exact permutation test.

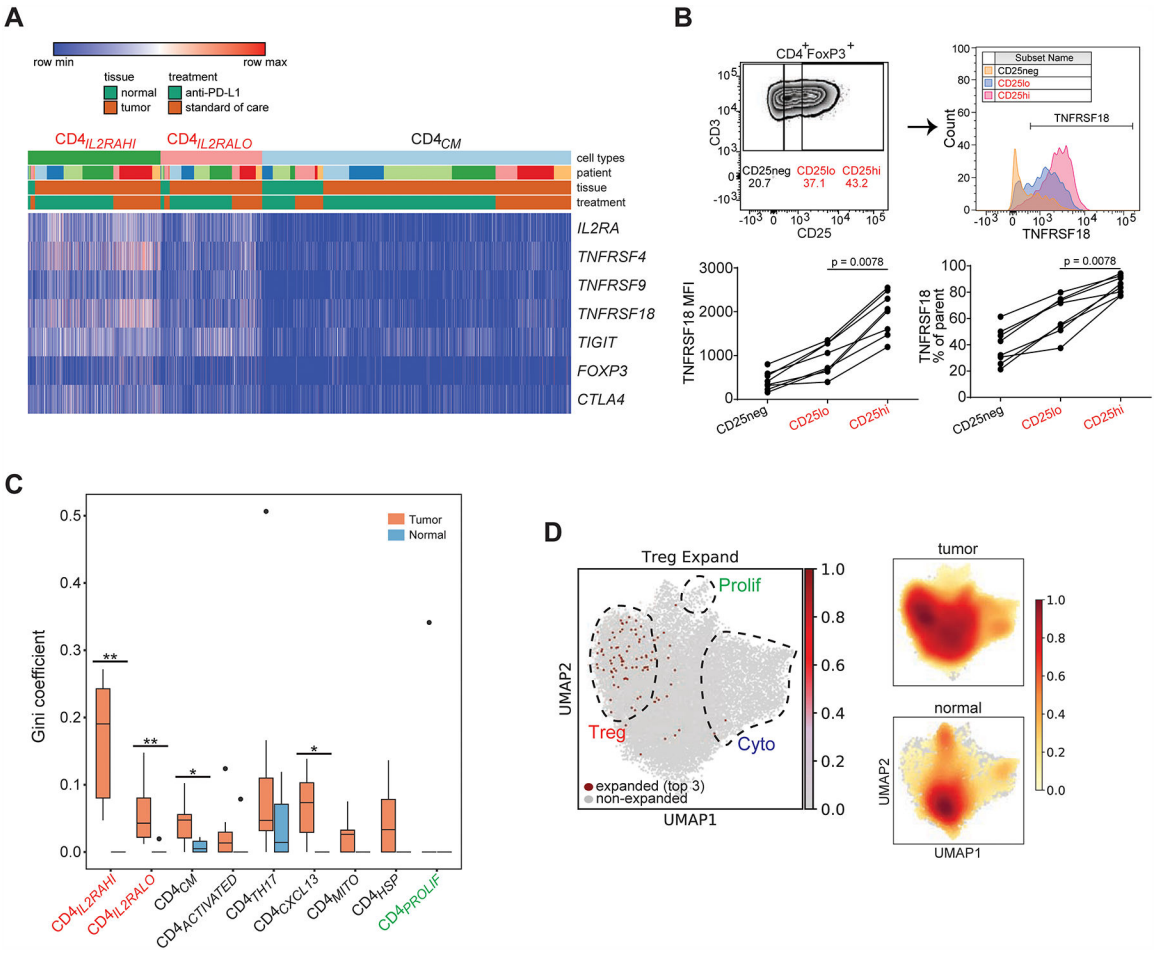

Figure 3. Regulatory CD4$^+$ T cells are heterogeneous, enriched and clonally expanded in bladder tumors.

(A) Heatmap shows the expression of select regulatory T cell marker genes (rows) for individual single cells (columns) within the CD4$_{IL2RAHI}$ and CD4$_{IL2RLO}$ clusters, compared to the CD4$_{CM}$ cluster. Cells were grouped based on their annotations by tissue (tumor or non-malignant), treatment, and patient. Log$_2$-transformed expression of each gene was row scaled. (B) Flow cytometry staining of CD4$^+$ FOXP3$^+$ tumor-infiltrating lymphocytes from a bladder tumor shows the gating strategy for CD25^{neg}, CD25^{low} and CD25^{hi} (upper left), and histograms of TNFRSF18 staining from each CD25 gate (upper right). Mean fluorescence intensity of TNFRSF18 and % TNFRSF18$^+$ from the parental gate are shown for CD25 gates across samples (N = 7 tumors, mean + s.e.m.). *, P < 0.05 by Wilcoxon paired T test. (C) Gini coefficients for regulatory populations (CD4$_{ILRA2HI}$, CD4$_{IL2RALO}$, red labels at far left) and other CD4$^+$ T cell populations within tumor and non-malignant compartments across all samples (*, P < 0.05, **, P < 0.01 by exact permutation test). N = 7 tumor samples; 6 non-malignant samples. (D) Left, single cells expressing the top 3 most expanded clonotypes found in the combined regulatory populations (CD4$_{ILRA2HI}$, CD4$_{IL2RALO}$) are shown in red in the same UMAP space as Figure 2A. The regions composed of regulatory, cytotoxic, and proliferating T cells are outlined and superimposed upon the UMAP

projection. Right, density plots for total $CD4^+$ T cell distribution within tumor and non-malignant compartments are reproduced from Figure 2D for ease of visual comparison.

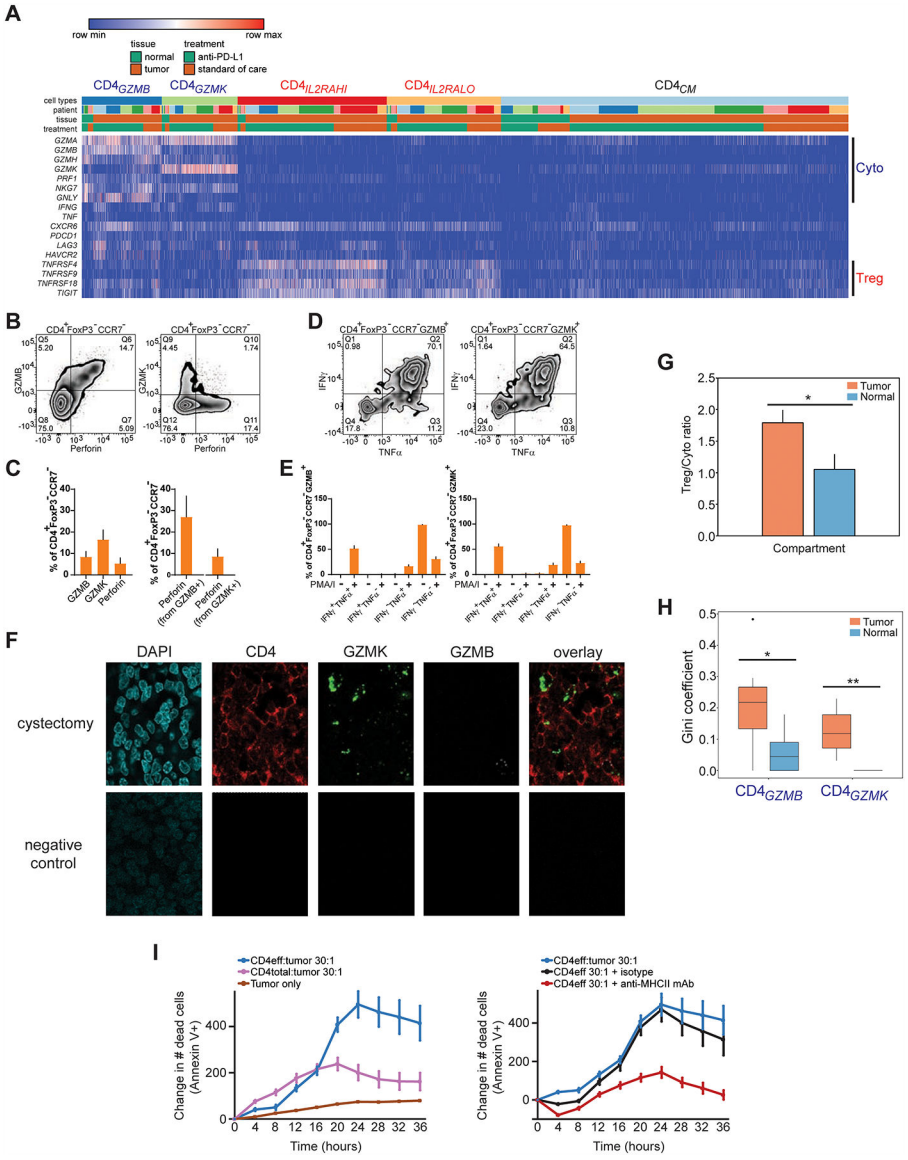

Figure 4. Multiple cytotoxic CD4$^+$ T cell states are enriched and clonally expanded in bladder tumors, and possess lytic capacity against tumors.

(A) Heatmap shows the expression of select cytotoxic or regulatory T cell marker genes (rows) for individual single cells (columns) within the cytotoxic CD4$_{GZMB}$ and CD4$_{GZMK}$ clusters, compared to regulatory (CD4$_{IL2RAHI}$, CD4$_{IL2RLO}$) and CD4$_{CM}$ clusters. Cells were grouped based on their annotations by tissue (tumor or non-malignant), treatment, and patient. Log_2-transformed expression of each gene was row scaled. (B) Flow cytometry staining of GZMB, perforin, or GZMK in CCR7$^-$ CD4$^+$ FOXP3$^-$ T cells is shown. (C) Percentage of cells expressing GZMB, GZMK, or perforin from CCR7$^-$ CD4$^+$ FOXP3$^-$ T cells by flow cytometry (left), and the percentage of cells co-expressing perforin within GZMB$^+$ or GZMK$^+$ CCR7$^-$ CD4$^+$ FOXP3$^-$ T cells (right), are shown (N = 7 tumors, mean + s.e.m.). (D) Representative flow cytometry staining of IFNγ and TNFα expression in GZMB$^+$ or GZMK$^+$ CCR7$^-$ CD4$^+$ FOXP3$^-$ T cells stimulated with PMA and ionomycin. Bottom row, percentages of cells expressing IFNγ, TNFα, or both from GZMB$^+$ or GZMK$^+$

CCR7^{-} CD4^{+} FOXP3^{-} T cells with and without stimulation (N = 11 tumors, mean + s.e.m.). (F) Multiplex immunofluorescent staining of DAPI (blue), CD4 (immunohistochemistry, red), *GZMK* (RNAscope probe, green), *GZMB* (RNAscope probe, white) and overlay without DAPI are shown from a cystectomy tumor region from a patient with parallel scRNA-seq and TCR-seq data (anti-PD-L1 C, top row), and from a corresponding tumor field with negative control staining (bottom row). CD4^{+} cells that co-express *GZMK* (arrows) or *GZMB* (arrowhead) are indicated. Scale bar, 10 μm. (G) The ratio of abundances of all regulatory T cell populations (CD4$_{ILRAHI}$, CD4$_{IL2RALO}$) to all cytotoxic CD4^{+} populations (CD4$_{GZMB}$, CD4$_{GZMK}$) across all tumor and non-malignant samples is shown. (*, $P < 0.05$ by unpaired T test assuming unequal variance.) (H) Gini coefficients for each of the cytotoxic CD4^{+} populations within tumor and non-malignant compartments across all samples (*, $P < 0.05$, **, $P < 0.01$, exact permutation test. N = 7 tumor samples, 6 non-malignant samples.) (I) Left panel, quantitation of Annexin V^{+} apoptotic cells over time from a time-lapse cytotoxicity experiment with tumor cells cultured alone or with either bulk CD4^{+} TIL (CD4$_{total}$) or CD4^{+} TIL depleted of regulatory T cells (CD4$_{eff}$) at 30:1 effector:target ratio. Right panel, CD4$_{eff}$ TIL and tumor cells (30:1 effector:target ratio) were co-cultured with a pan-anti-MHCII antibody or isotype control. All traces were from the same culture and cytotoxicity assay from the same patient. All traces show relative change in cell death from timepoint 0. Cytotoxicity with CD4$_{eff}$ are representative of independent experiments from 4 different patients. Mean ± s.e.m. from multiple technical replicates for each experiment are shown.

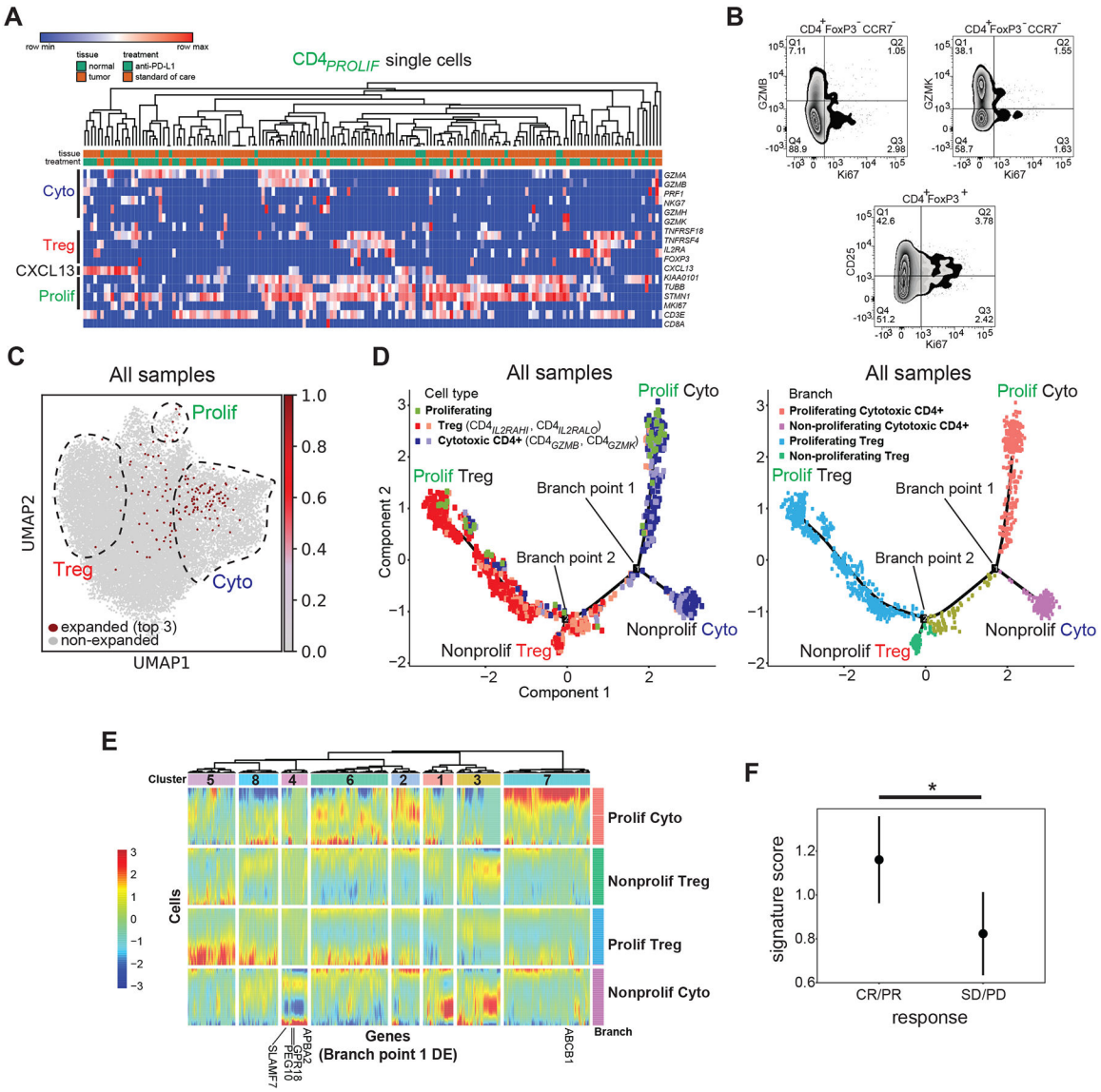

Figure 5. Proliferating CD4$^+$ T cells contain both regulatory and cytotoxic cell states.

(A) Heatmap showing expression of select cytotoxic, regulatory, and proliferating marker genes (rows) for individual single cells (columns) within the CD4$_{PROLIF}$ cluster. Samples were hierarchically clustered. Log$_2$-transformed expression of each gene was row scaled. (B) Representative flow cytometry staining from a bladder tumor showing expression of CD25, GZMB, GZMK, and Ki67. (C) Single cells expressing the top 3 most expanded clonotypes found in the CD4$_{PROLIF}$ T cell population are shown in red in the same UMAP space as Figure 2A. The regions composed of proliferating, regulatory, and cytotoxic T cells are outlined and superimposed upon the UMAP projection for visualization. (D) Left panel, pseudotime trajectories derived from all tumors (N = 7 samples) and non-malignant samples (N = 6 samples). Cells with expanded TCRs from the proliferating (CD4$_{PROLIF}$, green), regulatory (CD4$_{IL2RAHI}$, CD4$_{IL2RALO}$, shades of red), and cytotoxic (CD4$_{GZMB}$, CD4$_{GZMK}$, shades of purple) states were used for this analysis. Specific branches corresponding to proliferating cytotoxic cells (upper right), non-proliferating cytotoxic cells (lower right),

proliferating regulatory cells (upper left), and non-proliferating regulatory cells (lower left) are labeled. Right panel, branches are color coded according to the above proliferating or non-proliferating identities. Also labeled are branch points that discriminate proliferating and non-proliferating cytotoxic $CD4^+$ T cells (branch point 1), and proliferating and non-proliferating regulatory T cells (branch point 2). (E) Heatmap showing all differentially expressed genes (columns) between branches for branch point 1, across cells in the pseudotime analysis (rows). Cells are grouped by their proliferating or non-proliferating branch assignments, color-coded at the right of the heatmap and corresponding to colors in (D). Genes are grouped by color-coded clusters (1–8) shown at the top of the plot, which result from hierarchical clustering based on co-regulation in specific branches. (F) Cytotoxic $CD4^+$ T cell gene signature scores were plotted in clinical responders (complete response or partial response) vs non-responders (stable disease or progressive disease) from baseline metastatic biopsies from bladder cancer patients with inflamed tumors on the IMvigor210 clinical trial (N = 62 tumors). Signature score was obtained from the IMvigor210 bulk RNA-seq data set for the cytotoxic $CD4^+$ T cell-specific genes derived from non-proliferating (cluster 4) and proliferating (cluster 7) cytotoxic $CD4^+$ clusters from pseudotime analysis shown below the heatmap in (E). Median ± s.e.m. shown. *, P = 0.037 by two-tailed T test.

KEY RESOURCES TABLE

REAGENT or RESOURCE	SOURCE	IDENTIFIER
Antibodies		
Brilliant Violet 605 CD25, clone BC96	Biolegend	Cat# 302632
Brilliant Violet 786 CD127, clone A019D5	Biolegend	Cat# 351330
Brilliant Violet 421 CD4, clone OKT4	Biolegend	Cat# 317434
Brilliant Violet 650 CD3, clone UCHT1	Biolegend	Cat# 300468
Brilliant Ultraviolet 395 CD45, clone H130	Becton Dickinson	Cat# 563792
Alexa Fluor 647 CD8, clone SK1	Biolegend	Cat# 344726
FITC GZMK, clone GM26E7	Biolegend	Cat# 370508
PerCP-Cy5.5 HLA-DR, clone L243	Biolegend	Cat# 307630
APC-R700 CCR7, clone 3D12	Becton Dickinson	Cat# 565867
Brilliant Violet 480 CD3, clone UCHT1	Becton Dickinson	Cat# 566105
Brilliant Violet 510 GZMB, clone GB11	Becton Dickinson	Cat# 563388
Brilliant Violet 605 Ki67, clone Ki-67	Biolegend	Cat# 350522
Brilliant Violet 650 CD45RA, clone HI100	Biolegend	Cat# 304136
Brilliant Violet 786 CD25, clone BC96	Biolegend	Cat# 302638
Brilliant violet 711 TNFSRF18, clone 108–17	Biolegend	Cat# 371212
Brilliant ultraviolet 395 CD4, clone RPA-T4	Becton Dickinson	Cat# 564724
Brilliant ultraviolet 496 CD8, clone RPA-T8	Becton Dickinson	Cat# 564808
Brilliant ultraviolet 805 CD45, clone HI30	Becton Dickinson	Cat# 564914
PE-CF594 FoxP3, clone 259D/C7	Becton Dickinson	Cat# 562421
PE-Cy7 Perforin, clone B-D48	Biolegend	Cat# 353316
Alexa Fluor 647 IFNγ, clone 4S.B3	Biolegend	Cat# 502516
PE anti-human TNFα, clone Mab11	Biolegend	Cat# 502909
CD4, clone SP35	Cell Marque	Cat# 104R-18
Alexa Fluor 555 goat anti-rabbit IgG(H+L)	Invitrogen	Cat# 4050–32
Chemicals, Peptides, and Recombinant Proteins		
Liberase TL, research grade	Millipore Sigma	Cat# 5401020001
Draq7	Biolegend	Cat# 424001
Live/dead fixable Near-IR dead cell stain	Invitrogen	Cat# L34975
FluoroFix buffer	Biolegend	Cat# 422101
Recombinant human IL-2	Peprotech	Cat# 200–02
IncuCyte Annexin V Red reagent	Essen Bioscience	Cat# 4641
IncuCyte Cytotox Red reagent	Essen Bioscience	Cat# 4632
RNAscope probe, Homo sapiens, *GZMB* (channel 2)	Advanced Cell Diagnostics	Cat# 445971-C2
RNAscope probe, Homo sapiens, *GZMK* (channel 1)	Advanced Cell Diagnostics	Cat# 475901-C1
L15 media, 15 mM HEPES, 600 mg% glucose	UCSF Cell Culture Facility	N/A
Fetal bovine serum	Omega Scientific	Cat# FB-01

REAGENT or RESOURCE	SOURCE	IDENTIFIER
RPMI-1640	UCSF Cell Culture Facility	N/A
ImmunoCult XF complete medium (Medium + 10% FCS + 1% penicillin / streptomycin)	STEMCELL Technologies	Cat# 10981
Critical Commercial Assays		
GentleMACS	Miltenyi Biotec	Cat# 130-093-235
FoxP3/transcription factor staining buffer set	eBioscience	Cat# 00-5523-00
Cell stimulation cocktail	eBioscience	Cat# 00–4975
Chromium™ Single Cell 3' Library, Gel Bead & Multiplex Kit	10X Genomics	Cat# 120233 (discontinued)
Chromium™ Single Cell 3' Chip Kit	10X Genomics	Cat# 120232 (discontinued)
Dynabeads Human T-Activator CD3/CD28/CD137	Gibco	Cat# 11162D
Opal 7-color manual IHC kit	Perkin Elmer	Cat# NEL811001KT
Deposited Data		
Processed data	This study	NCBI GEO: GSE149652
Healthy human donor TCR data for $CD4^+$ peripheral blood mononuclear cells	10X Genomics	https://support.10xgenomics.com/single-cell-vdj/datasets/2.2.0/vdj_v1_hs_cd4_t
Healthy human donor TCR data for $CD8^+$ peripheral blood mononuclear cells	10X Genomics	https://support.10xgenomics.com/single-cell-vdj/datasets/2.2.0/vdj_v1_hs_cd8_t
Human reference genome, build hg19	10X Genomics	https://software.10xgenomics.com
Oligonucleotides		
TCR sequencing primers	Table S3	N/A
Software and Algorithms		
Cell Ranger v1.1	10X Genomics	https://software.10xgenomics.com
Scanpy v1.4.3	Wolf et al., 2018	https://scanpy.readthedocs.io/en/stable/index.html
miXCR v2.1.12	Bolotin et al., 2015	https://mixcr.readthedocs.io/en/latest/
Monocle v2.10.1	Qiu et al., 2017	Bioconductor
SingleR v1.1.9	Aran et al., 2019	Bioconductor
FlowJo	TreeStar	N/A